

1 Aerosol radiative effects in the ultraviolet, visible, and near-infrared spectral ranges using long-term  
2 aerosol data series over the Iberian Peninsula

3

4 D. Mateos<sup>1,2</sup>, M. Antón<sup>1</sup>, C. Toledano<sup>2</sup>, V. E. Cachorro<sup>2</sup>, L. Alados-Arboledas<sup>3,4</sup>, M. Sorribas<sup>3,4,5</sup>,  
5 M.J. Costa<sup>6</sup>, J.M. Baldasano<sup>7</sup>.

6 1. Departamento de Física, Universidad de Extremadura, Badajoz, Spain

7 2. Grupo de Óptica Atmosférica, Universidad de Valladolid, Valladolid, Spain

8 3. Departamento de Física Aplicada, Universidad de Granada, Granada, Spain

9 4. Andalusian Institute for Earth System Research, Universidad de Granada, Granada, Spain

10 5. Estación de Sondeos Atmosféricos El Arenosillo, INTA, Huelva, Spain

11 6. Évora Geophysics Centre and Dep. Physics, University of Évora, Évora, Portugal

12 7. Universidad Politécnica de Cataluña, Barcelona, Spain

13

14 Corresponding author: D. Mateos, Grupo de Óptica Atmosférica, Universidad de Valladolid, Paseo

15 Belén 7, 47011, Valladolid, Spain. E-mail: mateos@goa.uva.es

16

17

18

19

20 **Abstract**

21 A better understanding of the aerosol radiative properties is a crucial challenge for climate change  
22 studies. This study aims to provide a complete characterization of aerosol radiative effects in  
23 different spectral ranges within the shortwave (SW) solar spectrum. For this purpose, long-term  
24 datasets of aerosol properties from six AERONET stations located in the Iberian Peninsula  
25 (Southwestern Europe) are analyzed in term of climatological characterization and trends. Aerosol  
26 information is used as input to the libRadtran model in order to determine the aerosol radiative  
27 effect at the surface in the ultraviolet ( $ARE_{UV}$ ), visible ( $ARE_{VIS}$ ), near-infrared ( $ARE_{NIR}$ ), and the  
28 entire SW range ( $ARE_{SW}$ ) under cloud-free conditions. Over the whole Iberian Peninsula, yearly  
29 aerosol radiative effects in the different spectral ranges are:  $-1.1 < ARE_{UV} < -0.7 \text{ W m}^{-2}$ ,  $-5.7 <$   
30  $ARE_{VIS} < -3.5 \text{ W m}^{-2}$ ,  $-2.6 < ARE_{NIR} < -1.6 \text{ W m}^{-2}$ , and  $-8.8 < ARE_{SW} < -5.7 \text{ W m}^{-2}$ . Monthly  
31 means of ARE show a seasonal pattern with larger values in spring and summer. The aerosol  
32 forcing efficiency (AFE), ARE per unit of aerosol optical depth, is also evaluated in the four  
33 spectral ranges. AFE exhibits a dependence on single scattering albedo and a weaker one on  
34 Ångström exponent. AFE is larger (in absolute value) for small and absorbing particles. The  
35 contributions of the UV, VIS, and NIR ranges to the SW efficiency vary with the aerosol types.  
36 Aerosol size determines the fractions of  $AFE_{VIS}/AFE_{SW}$  and  $AFE_{NIR}/AFE_{SW}$ . VIS range is the  
37 dominant region for all types, although non-absorbing large particles cause a more equal  
38 contribution of VIS and NIR intervals. The  $AFE_{UV}/AFE_{SW}$  ratio shows a higher contribution for  
39 absorbing fine particles.

40

41

## 42 **1. Introduction**

43 Atmospheric aerosol particles can absorb and scatter part of the total amount of solar radiation  
44 entering the Earth's atmosphere. In fact, aerosols directly influence the Earth's energy budget and  
45 act as cloud condensation nuclei modifying the cloud structure (e.g., Boucher et al., 2013). Aerosols  
46 can either be produced by ejection into the atmosphere or by physical and chemical processes  
47 within the atmosphere. Aerosol particles affect the radiative field by attenuating the direct  
48 component thereby enhancing (or reducing under a highly absorbing aerosol) the diffuse one. They  
49 also produce indirect effects by perturbing the Earth's atmospheric radiative balance by modulating  
50 cloud albedo and fraction.

51 The aerosol radiative effect (ARE) is defined as the change in net radiation due to changes in  
52 atmospheric aerosol properties and content. This is a key quantity in the determination of climate  
53 change (e.g., Hansen et al., 1998). Most studies dealing with ARE have focused on discrete  
54 wavelengths, whole shortwave (SW) solar radiation spectrum (e.g., Rajeev and Ramanathan, 2001;  
55 García et al., 2008; di Sarra et al., 2008; Foyo-Moreno et al., 2014; Mateos et al., 2013a), longwave  
56 (LW) radiation (e.g., Panicker et al., 2008; di Sarra et al., 2011; Antón et al., 2014), ultraviolet (UV)  
57 interval (e.g., Hatzianastassiou et al., 2004; Kazadzis et al., 2009; Nikitidou et al., 2013), and visible  
58 (VIS) range (e.g., Jayaraman et al., 1998; Horvath et al., 2002; Bush and Valero, 2003; Meloni et  
59 al., 2003). With regards to surface SW radiative effect ( $ARE_{SW}$ ), Di Biagio et al. (2010) obtained  
60 the maximum radiative daily effects for different aerosol types in the central Mediterranean in the  
61 period 2004-2007:  $-61 \text{ Wm}^{-2}$  (desert dust aerosols),  $-26 \text{ Wm}^{-2}$  (urban/industrial - biomass burning  
62 aerosols) and  $-43 \text{ Wm}^{-2}$  (mixed aerosols). All these negative figures point out a cooling of the  
63 Earth's surface. Aerosol radiative effects in the LW range ( $ARE_{LW}$ ) for dust particles are expected  
64 to be smaller than in the SW and with positive sign (see, e.g., di Sarra et al., 2011; Antón et al.,  
65 2014). Hence, this heating effect at the surface can partly offset the cooling induced in the SW

66 range. With respect to the ARE for the UV range ( $ARE_{UV}$ ), Nikitidou et al. (2013) analyzed the  
67 ARE in two different spectral regions in the UV range, 300-315 and 315-360 nm. They found a  
68 stronger attenuation in the UV-B than in the UV-A.

69 The main goal of this study is to evaluate the ARE at the surface over the Iberian Peninsula, which  
70 is a region of great interest because of its geographical position in Southwestern Europe, near the  
71 African continent and the interface between the Atlantic Ocean and the Mediterranean Basin. Thus,  
72 it is affected by frequent desert dust intrusions which modulate their aerosol climatology (Toledano  
73 et al., 2007a, Bennouna et al., 2011; Pey et al., 2013; Valenzuela et al., 2012). In addition, this area  
74 is also affected by a great variety of air masses loaded with different aerosol types: clean  
75 continental, polluted plumes of central Europe, and marine aerosols. Hence, aerosol climatology at  
76 six stations (Palencia, Barcelona, Cabo da Roca, Évora, Granada, and El Arenosillo) is also carried  
77 out for different time periods between 2001 and 2012. Aerosol radiative effects as well as their  
78 efficiency are calculated in four regions of the solar spectrum (ultraviolet, visible, near-infrared, and  
79 shortwave) and the relative contribution of each range with respect to the whole solar spectrum is  
80 analyzed as a function of the aerosol properties. Therefore, this study is intended to contribute to the  
81 understanding of the aerosol impact on radiative budget over the Iberian Peninsula.

82 This article presents the following outline: detailed descriptions of the aerosol stations and the  
83 database used are performed in Section 2; Section 3 includes the followed methodology; the results  
84 obtained in the different analyses about the climatology of aerosol properties, aerosol radiative  
85 effects, and aerosol forcing efficiencies are shown and discussed in Sections 4,5, and 6,  
86 respectively. Finally, the main conclusions of this article are summarized in Section 7.

87

88

## 89 **2. Columnar aerosol optical data**

90 The aerosol data are obtained from the Aerosol Robotic Network (AERONET) (Holben et al.,  
91 1998). Six AERONET sites operating in the Iberian Peninsula are selected in this study: Palencia,  
92 Barcelona, Évora, Cabo da Roca, Granada and El Arenosillo (see Table 1), all of them with a  
93 minimum of 8 years of data sets of continuous observations. These sites present the largest records  
94 of aerosol properties in the Iberian Peninsula in the AERONET network.

95 The standard instrument used in AERONET is the Cimel CE-318 radiometer. It performs direct sun  
96 measurements at several wavelengths in the spectral range 340-1020 nm. Furthermore, the  
97 instrument also measures sky radiance in the solar almucantar and principal plane configurations at  
98 440, 670, 870 and 1020 nm wavelengths. A detailed description of this instrument was provided by  
99 Holben et al. (1998). The direct sun observations are used to derive the spectral aerosol optical  
100 depth (AOD) and the corresponding Ångström exponent. The sky radiances together with the AOD  
101 are employed to retrieve a set of aerosol optical and microphysical properties via inversion methods  
102 (Dubovik and King, 2000; Dubovik et al., 2006). These include particle size distribution, complex  
103 refractive index, single scattering albedo (SSA), phase function, asymmetry parameter, fraction of  
104 non-spherical particles, etc. (see  
105 [http://aeronet.gsfc.nasa.gov/new\\_web/Documents/Inversion\\_products\\_V2.pdf](http://aeronet.gsfc.nasa.gov/new_web/Documents/Inversion_products_V2.pdf)). Data are provided  
106 in three database levels: 1.0 (raw data), 1.5 (cloud-screened) and 2.0 (cloud-screened and quality  
107 assured).

108 The calibration of these instruments is performed following AERONET protocols by AERONET-  
109 NASA, PHOTONS and RIMA networks every 12 months of operation approximately. The  
110 estimated uncertainty is 0.01-0.02 for AOD (larger at shorter wavelengths) and ~5% for the sky  
111 radiances (Holben et al., 1998). The SSA has an absolute uncertainty about 0.03-0.07 depending on  
112 the aerosol load and type (Dubovik et al., 2000).

113 Level 2.0 aerosol optical depth data have been used in this work. However, it is well-known that  
114 when level 2.0 inversion data are used, the number of available observations of single scattering  
115 albedo (SSA) and asymmetry factor ( $g$ ) is quite limited because these variables are only considered  
116 reliable when  $AOD_{440nm} > 0.4$ <sup>1</sup>. Such AOD is mainly reached in the study region during Saharan  
117 dust or biomass burning events, therefore we would not have information on SSA and  $g$  for other  
118 conditions. To solve this issue, we have reduced the threshold of the level 2.0 inversion products.  
119 For this, we started with the level 1.5 data (for those quality-assured almucantar data that reached  
120 level 2.0) and applied the same criteria used by AERONET to elaborate the level 2.0 regarding the  
121 number of symmetrical angles, retrieval error and solar zenith angle (see  
122 [http://aeronet.gsfc.nasa.gov/new\\_web/Documents/AERONETcriteria\\_final1\\_excerpt.pdf](http://aeronet.gsfc.nasa.gov/new_web/Documents/AERONETcriteria_final1_excerpt.pdf)).  
123 However, a less restrictive threshold is applied to the AOD, which we restricted to cases with  
124  $AOD_{440nm} > 0.15$ , instead of 0.4. This choice must be considered a compromise between the amount  
125 and the quality of the data. This kind of approach has been adopted by other authors using  
126 AERONET absorption data (e.g. Mallet et al., 2013). The threshold of 0.15 seems adequate  
127 analyzing the typical values of the AOD in the Iberian Peninsula (e.g., Bennouna et al., 2011;  
128 Obregón et al., 2012), because it can be considered a value to separate background aerosol  
129 conditions from episodic events with moderate or high aerosol loadings. The level 1.5-filtered data  
130 of SSA and  $g$  are daily averaged in order to have one value per day. In these conditions, the  
131 estimated uncertainty of the single scattering albedo is  $\pm 0.05-0.07$  (Dubovik et al., 2000).  
132 Furthermore, for those days presenting level 2.0 data but also measurements in the 1.5-filtered level,  
133 we tested the uncertainty of our approach. We evaluated the difference in the SSA values of the  
134 level 1.5-filtered data with respect to the closest level 2.0 data. The mean relative differences in the

---

<sup>1</sup> Other inversion products, like the volume size distributions, are provided for all AOD levels.

135 SSA values between both methodologies are smaller than 1%, being in the same order that the  
136 inversion uncertainty.

137 Lastly, when the AOD is low ( $<0.15$  at 440 nm), there is no reliable information on the absorption  
138 properties in the almucantar retrievals. Such low AOD is typical in our study region (e.g. almost  
139 70% of observations at Palencia, Granada and Évora are below this threshold). If only cases with  
140  $AOD_{440nm} > 0.15$  are considered in our study, the derived aerosol radiative effect would be  
141 unrealistically large. To overcome this problem of representativeness, fixed values of SSA (0.90)  
142 and  $g$  (0.75) have been used for the cases with  $AOD < 0.15$  at 440 nm, considering typical values  
143 for continental, desert, and maritime aerosols (e.g., Hess et al., 1998). In spite of the associated  
144 uncertainties, our approximation (daily level 1.5-filtered values of these aerosol properties for AOD  
145  $> 0.15$  together with a typical fixed value for low AOD cases) provides a good characterization of  
146 the aerosol absorption of the particles present in the atmosphere. The data products and AERONET  
147 database level are summarized in Table 2, where the estimated absolute uncertainties of AOD and  
148 SSA are also provided.

149

### 150 **3. Methodology**

151 The ARE calculations are performed in the ultraviolet ( $ARE_{UV}$ , 280-400 nm), visible ( $ARE_{VIS}$ , 400-  
152 700 nm), near-infrared ( $ARE_{NIR}$ , 700-2800 nm), and shortwave ( $ARE_{SW}$ , 280-2800 nm) intervals.  
153 For this purpose, cloud-free simulations are carried out by means of a radiative transfer code.

154 The libRadtran model (Mayer and Kylling, 2005) has been shown to be a useful tool for obtaining  
155 solar radiation data, presenting high accuracy (e.g., Román et al., 2014). Version 1.7 of the  
156 libRadtran is used in this study with inputs of aerosol, total ozone column (TOC), precipitable water  
157 vapor column (PWC), and surface albedo data. We performed simulations of ultraviolet (280-400

158 nm), visible (400-700 nm), near-infrared (700-2800 nm), and shortwave (280-2800 nm) radiation  
159 during the periods indicated in Table 1. Total ozone column is provided by the Ozone Monitoring  
160 Instrument (OMI) and Total Ozone Mapping Spectrometer (TOMS). Daily values of these  
161 instruments are obtained from the Daily Level 3 Global Gridded products, which are downloaded  
162 using the Giovanni application (<http://disc.sci.gsfc.nasa.gov/giovanni>). Level 2.0 AERONET PWC  
163 data are used in the calculations. The uncertainty of this parameter is 10-15% (Holben et al., 1998).  
164 In addition, retrievals of surface albedo at 440, 675, 870 and 1020 nm from the AERONET  
165 algorithm are also used in this work. For land surface cover, this algorithm relies on the Lie–Ross  
166 model (Lucht and Roujean, 2000), but considering the bidirectional reflectance distributions from  
167 MODIS (Moody et al., 2005).

168 Aerosol properties obtained from AERONET measurements are also used as input to the libRadtran  
169 model. Ångström coefficients,  $\alpha$  and  $\beta$ , are utilized to compute a spectral aerosol optical depth in  
170 the wavelengths of interest (Schuster et al., 2006). Ångström exponent  $\alpha$  is obtained with the  
171 measurements between 440 and 870 nm, while the turbidity  $\beta$  is obtained from the  $\alpha$  value and  
172 aerosol data at 1020 nm. Since the aerosol asymmetry factor, single scattering albedo, and surface  
173 albedo are obtained at four wavelengths from AERONET in each measurement, three different  
174 spectral regions are simulated with the libRadtran model. For computations in the UV range (280-  
175 400 nm), the AERONET retrievals of aerosol asymmetry factor, aerosol single scattering albedo,  
176 and surface albedo at 440 nm are used. The AERONET retrievals at 675 nm of the same variables  
177 are used in the visible range (400-700 nm), while in the near-infrared region (700-2800 nm) we  
178 used the average properties retrieved at 870 and 1020 nm. In each interval, these properties are  
179 considered as wavelength independent. This choice to perform the radiative transfer simulations is  
180 proven as adequate in the Appendix A. Other options in the model set-up are: extraterrestrial  
181 irradiance values are taken from Gueymard (2004); profiles of temperature, air density, ozone and  
182 other atmospheric gases are taken from the midlatitude summer/winter standard atmospheres; and



183 the radiative equation solver is the improved version of the discrete ordinate method of Stamnes et  
184 al. (2000) (DISORT2) calculated by 16-streams (e.g., de Miguel et al., 2011). After computing the  
185 solar irradiance in the different spectral intervals, the SW irradiance is evaluated by adding up the  
186 contributions of these three spectral regions.

187 In order to evaluate the aerosol radiative effect, the simulations under aerosol-free conditions are  
188 also computed with the same inputs as explained above, but with a fixed  $\beta$  value of 0.001.

189 The use of radiative transfer models fed with reliable experimental aerosol data to determine the  
190 ARE has been also employed in other studies (e.g., Barja and Antuña, 2011; Valenzuela et al., 2012;  
191 García et al., 2014).

192 Once the simulated radiometric values are obtained, ARE is derived for each interval (X represents  
193 UV, VIS, NIR, and SW) at the surface by:

194

$$195 \text{ ARE}_X = \left( X_{\text{aer}}^{\downarrow} - X_{\text{aer}}^{\uparrow} \right) - \left( X_{\text{NOaer}}^{\downarrow} - X_{\text{NOaer}}^{\uparrow} \right) \quad (1)$$

196

197 where  $X_{\text{aer}}$  and  $X_{\text{NOaer}}$  are the irradiances ( $\text{W m}^{-2}$ ) for the X range under actual and aerosol-free  
198 conditions, respectively.

199 Daily values are obtained by the integration of the hourly data during the whole day (24 h)  
200 considering  $\text{ARE} = 0 \text{ Wm}^{-2}$  for  $\text{SZA} > 90^\circ$  (e.g., Bush and Valero, 2003; Valenzuela et al., 2012)  
201 and assuming cloud-free conditions along the day:

202

$$\text{ARE}_{\text{daily}} = \sum \text{ARE}_{\text{hourly}} \frac{dt}{24} \quad (2)$$

203

204 The aerosol forcing efficiency (AFE) is defined as the rate at which the radiative effect varies per  
205 unit of AOD (e.g., Di Biagio et al., 2009; and the references therein). The linear relationship  
206 between aerosol radiative effect and AOD is well known (see, e.g., Costa et al., 2004, 2006; Di  
207 Biagio et al., 2009). Hence, in this study, ARE is obtained as the slope of linear fits in the ARE vs  
208 AOD<sub>500nm</sub> relationships. Therefore, AFE values are expressed in W m<sup>-2</sup> per AOD<sub>500nm</sub>-unit (Wm<sup>-2</sup>τ<sup>-1</sup>).  
209

210 With respect to the temporal trends calculated in this study, the Sen's method (Sen, 1968) is applied  
211 to evaluate the slope of a time series using the Mann-Kendall non parametric test to determine the  
212 significance of these rates. The Sen's method is not greatly affected by outliers and can be  
213 computed when there are gaps in the database (Collaud Coen et al., 2013). This is a common and  
214 adequate method in temporal trend evaluation (e.g., Sánchez-Lorenzo et al., 2013). The trends  
215 calculated in this study are obtained in the corresponding physical units per year. However, to unify  
216 notation with previous studies dealing with the radiative effect trends of clouds and aerosols (e.g.,  
217 Mateos et al., 2013b), the results are multiplied by 10 and expressed in physical units per decade. In  
218 this way, the trends are also easier to read.

219

#### 220 **4. Analysis of aerosol properties over the Iberian Peninsula**

221 A direct CIMEL retrieval (AOD at 440 nm) is selected to perform the climatological analysis  
222 because the estimations of AOD<sub>500nm</sub> (used in the ARE calculations) are obtained using  $\alpha$  values.  
223 Hence, we minimized the impact of other uncertainty sources in the AOD analysis. Besides, the  
224 results for AOD<sub>440nm</sub> and AOD<sub>500nm</sub> do not differ excessively. In order to identify the differences in  
225 the aerosol climatology over the six sites analyzed in this study, the monthly distribution of the

226 daily values of the  $AOD_{440nm}$  and  $\alpha$  are evaluated using the database mentioned in Table 1. All the  
227 available level 2.0 AERONET measurements are used in this section.

228 Figure 1 shows the climatology of the aerosol load by box whisker plots. Several conclusions can  
229 be drawn from this figure. The highest values of the AOD occur in Barcelona, as can be expected  
230 because it is a large city. With respect to the monthly average values (triangles in the figure), the  
231 central stations in the Iberian Peninsula (Palencia and Évora) exhibit  $AOD_{440nm}$  below 0.2, while the  
232 southern sites (Cabo da Roca, Granada, and El Arenosillo) show aerosol load over 0.2 during  
233 summer months. The  $AOD_{440nm}$  seasonal distribution is seen, with maximum values in summer and  
234 minimum ones in winter. However, the seasonality becomes more evident in the stations outside the  
235 central area of the Iberian Peninsula. The large differences between median and average values for  
236 some months evidence a large impact of high aerosol optical depth events on the monthly  
237 climatology. In this line, the bimodality of the monthly AOD climatology (with two maximum  
238 monthly means occurring in March and summer months) observed for the El Arenosillo site has  
239 been already reported by previous studies (e.g., Bennouna et al., 2011), and directly attributed to  
240 desert dust intrusions from the African continent.

241 To go further in the characterization,  $\alpha$  allows for a better understanding of the particle size over  
242 each site. Figure 2 shows the climatology of this variable over the six stations using also box  
243 whisker plots. Analyzing the monthly average means,  $\alpha$  values larger than one, indicative of the  
244 predominance of fine particles, are dominant over Barcelona, Palencia, and Évora. The other three  
245 stations (Cabo da Roca, Granada, and El Arenosillo) present monthly  $\alpha$  averages over and below 1,  
246 which means a larger variety of aerosol sizes over these stations. A seasonal dependence over  
247 Granada site is seen, with winter months dominated by fine particles and summer months by larger  
248 ones (see also Navas-Guzman et al., 2013). Values of  $\alpha$  present a large variability during summer  
249 which is indicative of the influence of different aerosol types including biomass burning events and

250 Saharan dust transport (e.g., Pérez-Ramírez, 2008). The monthly distribution of  $\alpha$  is symmetric with  
251 similar average and median values through the year for the six sites.

252 With the daily AOD and  $\alpha$  values, it is possible to classify the origin of the aerosol particles.  
253 Previous studies suggest different thresholds of AOD and  $\alpha$  (e.g., Hess et al., 1998; Pace et al.,  
254 2006; Toledano et al., 2007b). A simple classification, which can be used for the whole Iberian  
255 Peninsula, of aerosol type is carried out in this study. The threshold between fine and large particles  
256 is placed at  $\alpha = 1$ , while the situations with a high aerosol load are those with  $\text{AOD}_{440\text{nm}} > 0.2$ .  
257 Therefore, aerosol particles can be classified in four types: maritime ( $\text{AOD}_{440\text{nm}} < 0.2$  and  $\alpha < 1$ ),  
258 desert dust ( $\text{AOD}_{440\text{nm}} > 0.2$  and  $\alpha < 1$ ), continental clean ( $\text{AOD}_{440\text{nm}} < 0.2$  and  $\alpha > 1$ ), and  
259 continental polluted ( $\text{AOD}_{440\text{nm}} > 0.2$  and  $\alpha > 1$ ). Note that the limit of  $\text{AOD}_{440\text{nm}} < 0.2$  is arbitrary  
260 and this value could be adjusted according to the sites, which likely produce a different distribution  
261 in the pie diagrams. Actually, even close stations can present slight differences in the  $\alpha$ -AOD  
262 classification (see, e.g., Obregón et al. 2012). However it is not the aim of this work to provide an  
263 extensive aerosol climatology, but rather to demonstrate the great variety of air masses over Iberia  
264 which transport different aerosol types. Although other types, such as biomass burning or mixed  
265 aerosols, are placed in the boundaries of these types, this simple classification can provide  
266 information about the aerosol sources for the six sites. The classification used here is in line with  
267 the previous studies. For instance, Toledano et al., (2007b) proposed for El Arenosillo site similar  
268 thresholds (see their Table V), although they identified continental polluted aerosols with an  
269  $\text{AOD}_{440\text{nm}}$  larger than 0.35 and  $\alpha > 1.4$ . Pace et al., (2006) proposed at Lampedusa island (Central  
270 Mediterranean) a desert dust identification when  $\text{AOD}_{440\text{nm}} \geq 0.15$  and  $\alpha \leq 0.5$ .

271 Figure 3 shows pie diagrams with the frequency of occurrence of the four aerosol types. The six  
272 diagrams agree pointing at continental clean as the main type of aerosols over the Iberian Peninsula.  
273 In Barcelona, there is also an important contribution of continental polluted, since Barcelona is a

274 large coastal city with relevant pollution levels from vehicular and ship traffic (e.g., Reche et al.,  
275 2011). The influence of maritime aerosols is notable at El Arenosillo, Cabo da Roca, and Évora  
276 sites (see also e.g., Bennouna et al., 2011; Obregón et al., 2012). Furthermore, desert dust events are  
277 shown to be common in the Iberian Peninsula with a higher occurrence at Granada and El  
278 Arenosillo sites (the two closest points to the African continent and hence to the Saharan desert)  
279 (see also Toledano et al., 2007b; Guerrero-Rascado et al., 2009; Antón et al., 2012). For instance,  
280 the minimum values of  $\alpha$  obtained for Granada station during summer months are linked to the  
281 higher likelihood of desert dust events (Valenzuela et al., 2012), being sometimes associated with  
282 high aerosol loads (Córdoba-Jabonero et al., 2011). These results corroborate the findings obtained  
283 by previous studies about desert dust events over the Iberian Peninsula (see, e.g., Lyamani et al.,  
284 2005; Toledano et al., 2007b; Cachorro et al., 2008).

285 The inter-annual change of aerosol load can be established over the last decade in the Iberian  
286 Peninsula. The yearly values of  $AOD_{440nm}$  at the six sites are shown in Figure 4. The geographical  
287 distribution of AOD through the Spanish geography is observed in the figure. Barcelona site  
288 presents yearly values over  $\sim 0.2$ . Granada, El Arenosillo, and Cabo da Roca exhibit yearly means in  
289 the interval between 0.15 and 0.22, while the means for Palencia and Évora sites are slightly lower  
290 in the range 0.12-0.18. Analyzing the six sites together, the year of 2010 presents one of the  
291 minimum values of  $AOD_{440nm}$ , while the maximum averages seem to appear at the early 2000s. The  
292 different sampling of AOD measurements in the six sites can produce discrepancies because  
293 different events are or are not captured in each database. In addition, possible technical problems  
294 and meteorological conditions (CIMEL aerosol data are recorded under cloud-free skies) cause a  
295 non-equally distribution through the year. Overall, summer is the season with the largest  
296 contribution of data, followed by spring, autumn, and winter. Looking at the years with a large  
297 sampling ( $>200$  days in, at least, four stations), 2005, 2007, and 2011, all the features mentioned  
298 above are corroborated for these particular years. The minimum of 2010 occurs when two Southern

299 sites (El Arenosillo and Cabo da Roca) have not enough data to evaluate the yearly mean. Hence,  
300 we cannot ensure that the apparent minimum of AOD recorded that year is linked to global-scale  
301 phenomena or to more local conditions at the other sites. During 2010 a persistent negative phases  
302 of North Atlantic Oscillation (NAO) and Quasi Biennial Oscillation (QBO) indexes was observed  
303 (e.g., Steinbrecht et al., 2011), and the connection between air mass transport at global scale and  
304 particulate matter (at the surface) is proved by Pey et al., (2013) in the Eastern Iberian Peninsula.

305 With respect to the temporal change, the evolution of these yearly values seems to be weak, which  
306 can be attributed to the large variability observed in the mean values, affected by different  
307 conditions and phenomena. In spite of this, the evaluation of the trend rates (see Section 3 for  
308 details) produces the more statistically significant trend for the Barcelona site, where a decrease of  
309 the aerosol load of 0.09 AOD<sub>440nm</sub>-unit per decade is observed with a *p value* of 0.02. The *p values*  
310 for the other sites point out non-statistically significant trends (*p value* > 0.05). However, the sign of  
311 the temporal trends is negative for all of them. Hence, a slight reduction of the aerosol load over the  
312 Iberian Peninsula can be deduced since 2000 from the annual values. This result obtained in the  
313 Southeastern Europe is in line with the long-term analysis of AOD series performed in Northern  
314 Germany and Switzerland by Ruckstuhl et al. (2008). These authors highlight a strong decrease of  
315 aerosol load starting in 1985, while the values are stabilized since about 2000.

316 The reasons behind the decrease in the aerosol load since the early 2000s are a mixed of  
317 anthropogenic and natural sources. As was reported by Aas et al. (2013), the particulate matter  
318 (PM) emissions in the Iberian Peninsula have decreased around 25% between 2000 and 2011.  
319 Furthermore, observational PM data in different Spanish sites have also shown a decrease trend in  
320 the 2000s (e.g., Barmpadimos et al., 2012; Cusack et al., 2012; Pey et al., 2013; Bennouna et al.,  
321 2014; Mateos et al., 2014). This fact can be understood by the effect of the current economic crisis  
322 and the implementation of new environmental laws to control the pollution (e.g., Querol et al.,

2014). In addition, recent studies have shown that natural aerosols have also decreased in the last decade. For instance, Gkikas et al. (2013) reported, using satellite AOD estimations, that strong and extreme desert dust episodes in the Mediterranean decreased in the period 2000-2007 over land surfaces. This trend is understood due to the low spring and summer frequencies in 2005 and 2007 and the high frequencies in 2000 and 2003. As it was shown by Pey et al. (2013), one possible reason behind this trend is the atypical trajectories followed by the air masses emerging from North Africa in summer since 2006. Hence, both columnar and surface aerosols have pointed out a decrease in the aerosol load over the Iberian Peninsula, which has increased solar radiation levels reaching the surface in the 2000s (Mateos et al., 2014).

332

## 333 **5. Inter-annual and intra-annual evolution of ARE**

334 From the daily data, the yearly ARE for each station and spectral range is evaluated to analyze the  
335 inter-annual changes (see Figure 5). In spite of the high variability of the yearly values with large  
336 standard deviations (see the vertical bars for Palencia station in the figure), the radiative effects of  
337 atmospheric aerosols have slightly declined over the last years. The patterns of ARE in the UV,  
338 VIS, NIR, and SW ranges are similar, since the inter-annual changes are simultaneously observed in  
339 the four spectral intervals. With respect to the geographical distribution, Barcelona and Granada  
340 sites exhibit the largest effects (more negative ARE), which is in line with the large values of  
341  $AOD_{440nm}$  shown in Figure 4. The weakest aerosol effect (less negative ARE) is observed in  
342 Palencia and Évora sites, which is again linked to the lower yearly  $AOD_{440nm}$ .

343 To establish the general behavior of the ARE over the whole Iberian Peninsula, the yearly values  
344 using the six ground-based stations are evaluated. Only those years with, at least, simultaneous  
345 measurements at three sites are considered in these averages, and consequently, the time period is  
346 limited to 2004-2012. Figure 6 shows the evolution of the ARE and AOD at 500 nm for the entire

347 peninsula. The decline of the AOD for this mean series produces a consequent decrease in the  
348 aerosol radiative effect at the four spectral ranges. The temporal trends of these yearly values are  
349 evaluated, and all the trends shown in Figure 6 resulted with *p values* between 0.004 and 0.03.  
350 Overall,  $ARE_{SW}$  over the Iberian Peninsula increased  $3.6 \text{ W m}^{-2}$  per decade (*p value* = 0.028) while  
351 the aerosol reduced  $0.04 \text{ AOD}_{500\text{nm}}$ -unit per decade (*p value* = 0.006). Furthermore, this reduction in  
352 the radiative effects of the atmospheric aerosol over the Iberian Peninsula could partially contribute  
353 to the increase in the levels of SW radiation at the surface (the brightening phenomenon) in this  
354 region reported by, e.g., Sanchez-Lorenzo et al. (2013) and Mateos et al. (2013b).

355 The yearly aerosol radiative effects over the entire peninsula are in the ranges:  $-1.1 < ARE_{UV} < -0.7$   
356  $\text{W m}^{-2}$ ,  $-5.7 < ARE_{VIS} < -3.5 \text{ W m}^{-2}$ ,  $-2.6 < ARE_{NIR} < -1.6 \text{ W m}^{-2}$ , and  $-8.8 < ARE_{SW} < -5.7 \text{ W m}^{-2}$ .  
357 The larger contribution of the visible spectral region with respect to the whole solar spectrum was  
358 also noticed by Bush and Valero (2003), and this is expected since the maximum of shortwave  
359 radiation is found in this interval. The relationship between ARE and  $\text{AOD}_{500\text{nm}}$  is analyzed more in  
360 detail in Section 6, when the aerosol forcing efficiency is evaluated for each ground-based station.

361 In addition to the inter-annual changes, the intra-annual behavior is also analyzed. For this purpose,  
362 the annual cycle (12 monthly means) is evaluated for the six stations (see Figure 7). A seasonal  
363 pattern is seen in  $ARE_{UV}$  and  $ARE_{VIS}$ , and therefore,  $ARE_{SW}$ . However,  $ARE_{NIR}$  does not follow a  
364 seasonal pattern, particularly at the Évora and Palencia stations given that  $ARE_{NIR}$  remains nearly  
365 constant. Small differences among the six stations are observed in the annual cycle during the cold  
366 seasons. The aerosol radiative effects are stronger during summer months. This can be related to the  
367 higher likelihood of desert dust or biomass burning events over the Iberian Peninsula in these  
368 months (e.g., Cachorro et al., 2008; Valenzuela et al., 2012), as was mentioned above. This is  
369 corroborated by the increase of the differences among the stations during the warm season, likely  
370 due to the variability in the impact of the desert dust episodes which strongly depend on the



371 geographical location of each site. The higher occurrence of large aerosol loads during the warm  
372 seasons (see Figure 1), can explain the more negative ARE during summer and spring in Figure 7.  
373 For instance, the Barcelona station, with the largest values of  $AOD_{440nm}$ , is the bottom curve of each  
374 panel in Figure 7. Furthermore, the influence of mineral dust aerosol (with high aerosol optical  
375 depth) during these months also causes strong radiative effects, as was also reported by previous  
376 studies (e.g., Cachorro et al., 2008; Guerrero-Rascado et al., 2009; Antón et al., 2011; Román et al.,  
377 2013; García et al., 2014). In addition, the bimodality of the monthly AOD climatology mentioned  
378 in Section 4 has its impact on the radiative effects. The annual AOD cycle (see Figure 1, El  
379 Arenosillo site) causes the inverse monthly distribution of ARE with a first minimum in March.  
380 This effect is more clearly seen in  $ARE_{NIR}$  and  $ARE_{SW}$ .

381

## 382 **6. Aerosol radiative forcing efficiency in different spectral ranges**

383 The daily AFE values are calculated (following the methodology described in Section 3) in all the  
384 spectral ranges. AFE is a function of the aerosol optical properties, where both the aerosol particle  
385 size distribution and absorptive properties play a key role (e.g., Antón et al., 2011). As we assumed  
386 a fixed value of  $SSA = 0.90$  in the simulations with  $AOD_{440nm} < 0.15$  (see Table 2), the AFE is  
387 calculated only for those cases showing  $AOD_{440nm}$  larger than 0.15.

388 To identify the influence of  $SSA$  and  $\alpha$  on AFE, this variable is calculated for several intervals of  
389 each aerosol property. Four categories of single scattering albedo at 675 nm are established in the  
390 calculation of the AFE:  $1.0 \geq SSA_1 > 0.95$ ,  $0.95 \geq SSA_2 > 0.90$ ,  $0.90 \geq SSA_3 > 0.85$ , and  $0.85 \geq$   
391  $SSA_4 > 0.80$ . Furthermore, aerosol size is classified in three intervals:  $0 \leq \alpha_1 \leq 1$ ,  $1 < \alpha_2 \leq 1.5$ , and  
392  $1.5 < \alpha_3 \leq 2$ . Note that two intervals in the range of  $\alpha$  larger than 1 have been considered. One for  
393 median particles and another one for fine particles, because of the relevant importance of median  
394 size particle (continental or mixed aerosol aerosols types) over the Iberian Peninsula (see Figure 3).

395 Although the general classification between fine and coarse particles requires a more refined  
396 classification (Schuster et al.,2006; Prats et al., 2011), the more general intervals selected in this  
397 study are adequate to perform a study of the aerosol sizes at the six stations together.

398 Figure 8 shows the AFE obtained for the UV ( $AFE_{UV}$ ), VIS ( $AFE_{VIS}$ ), NIR ( $AFE_{NIR}$ ), and SW  
399 ( $AFE_{SW}$ ) ranges for all these intervals. The threshold to evaluate the average in each sub-interval is  
400 fixed at 10 data points. From these figures it is seen that, the stronger the absorption by aerosols, the  
401 stronger their forcing efficiency. That is a decrease in the absolute values of the AFE for increasing  
402 SSA and for all particle size. In general, the groups of non-absorbing particles exhibit a good  
403 agreement among the six stations (see, for instance, AFE values in all the spectral ranges in the  
404 interval  $1 < \alpha \leq 1.5$ ). Larger differences are obtained in the case of more absorbing aerosol particles.  
405 These can be understood because of the different types of aerosols presented over each site (see  
406 Section 4) and the different data numbers. The average AFE values over the whole Iberian  
407 Peninsula (considering the six stations together) are presented in Table 3 as a function of  $\alpha$  and  
408 SSA, separately. The role played by the aerosol size on AFE values is different in the three sub-  
409 intervals of the shortwave radiation.  $AFE_{UV}$  and  $AFE_{VIS}$  are larger (in absolute value) for fine  
410 particles, while the opposite occurs in the case of  $AFE_{NIR}$ . As a result of these mixed effects,  $AFE_{SW}$   
411 shows also a decrease in its values with increasing  $\alpha$ , but this effect is weaker than for the visible  
412 and ultraviolet parts. SSA exhibits a more dominant role. As was observed before, the most  
413 negative values are achieved for the most absorbing aerosols considered in this study (group 1 of  
414 SSA, see Table 3).

415 The average values of forcing efficiency obtained in this study (see Table 3) are in line with those  
416 found by other authors. Table 4 summarizes the results obtained by previous studies. It is difficult to  
417 assess some features in the comparison with previous reported AFE values, because of the different  
418 aerosol types, time periods and methods that are analyzed. Our study presents the evaluation of

419 ARE with six long-term databases of aerosol properties. In spite of that, the values shown in Table  
420 3 agree with those of Table 4, but the larger discrepancies are observed with the studies focusing on  
421 specific events. Our results match better with the results reported by, e.g., Zhou et al. (2005),  
422 Meloni et al. (2005), and Di Biagio et al. (2010). As was noticed by, e.g., Costa et al. (2004, 2006)  
423 and Di Biagio et al. (2010), AFE at the surface is larger (in absolute term) for aerosols characterized  
424 by smaller and absorbing particles. This result is corroborated by the findings shown in this study.  
425 Furthermore, as was pointed out by Di Biagio et al. (2010), the aerosol absorption is the dominant  
426 factor on AFE evaluated at the surface.

427 To evaluate the contribution of each spectral range with respect to the shortwave, the dependence of  
428 each AFE ratio (VIS to SW and NIR to SW) on SSA and  $\alpha$  is shown in Figure 9.  $AFE_{VIS}/AFE_{SW}$   
429 and  $AFE_{NIR}/AFE_{SW}$  ratios are shown in the figure since their contributions are the dominant.  
430  $AFE_{UV}/AFE_{SW}$  ratio can be obtained as 100% minus the sum of the percentage of the two other  
431 ranges. As expected, non substantial differences are observed in the behavior of the six stations  
432 considered in this study. The NIR contribution becomes more decisive for large particles ( $\alpha < 1$ ). It  
433 is expected that larger particles interact more with the longer wavelengths, while the smaller  
434 particles present more interaction with the shorter wavelengths. The presence of large particles with  
435 low SSA (high absorption) leads to a reduction of the  $AFE_{NIR}/AFE_{SW}$  ratio as well as an increase of  
436 the  $AFE_{VIS}/AFE_{SW}$  ratio. However, for non-absorbing (high SSA) large particles, the  
437  $AFE_{NIR}/AFE_{SW}$  ratio increases, and the contributions of the visible and infrared parts become more  
438 similar (both around ~40-50%). The difference between  $AFE_{VIS}/AFE_{SW}$  and  $AFE_{NIR}/AFE_{SW}$   
439 increases for intermediate - fine particles. For these particles, the  $AFE_{VIS}/AFE_{SW}$  ratio does not  
440 show a dependence on SSA. The smallest contribution of the NIR interval is around ~25% under  
441 strong absorbing aerosols and fine particles, while  $AFE_{VIS}/AFE_{SW}$  is still over 60%. For this case,  
442 the contribution of the ultraviolet range achieves a maximum of ~15%, being almost comparable

443 with the near infrared contribution. In summary, aerosol size determines the relevance of VIS-NIR  
444 ranges, while SSA plays a key role, particularly, for large particles.

445

## 446 **7. Conclusions**

447 Six long-term datasets of aerosol properties over the Iberian Peninsula were analyzed and used as  
448 input in a radiative transfer model to simulate ultraviolet, visible, near-infrared, and shortwave  
449 radiation. The aerosol radiative effect (ARE) and aerosol forcing efficiency (AFE) were calculated.  
450 The main conclusions are as follows:

451 1) The annual cycles of AOD and  $\alpha$  values of atmospheric aerosols over the six analyzed stations  
452 present high variability among them, emphasizing the inhomogeneity of the Iberian Peninsula,  
453 mainly due to the different aerosol types over each station. The Barcelona site presents the largest  
454 values of AOD, although Southern stations (Granada and El Arenosillo sites) frequently exhibit  
455 daily values over 0.2 during summer months. The classification  $\alpha$ -AOD has shown that continental  
456 (mainly, clean) is the principal type of aerosol over the Iberian Peninsula. However, maritime  
457 aerosols are also common in the Cabo da Roca, El Arenosillo and Évora sites. Desert dust events  
458 are registered at the six sites, with the highest frequency at Granada and El Arenosillo, but the most  
459 relevant feature is the South-North gradient of desert dust load which modulates the aerosol  
460 climatology over the Iberian Peninsula.

461 2) In the whole Iberian Peninsula, yearly  $ARE_{UV}$  ranges between  $-1.1$  and  $-0.7 \text{ Wm}^{-2}$ ,  $ARE_{VIS}$   
462 ranges between  $-5.7$  and  $-3.6 \text{ Wm}^{-2}$ , and  $ARE_{NIR}$  has values between  $-2.6$  and  $-1.6 \text{ Wm}^{-2}$ . As a  
463 result,  $ARE_{SW}$  is in the range between  $-8.8$  and  $-5.7 \text{ Wm}^{-2}$ . The temporal trends of  $ARE_{UV}$ ,  $ARE_{VIS}$ ,  
464  $ARE_{NIR}$ , and  $ARE_{SW}$  exhibit positive statistically significant trends between 2004 and 2012. For  
465 instance, the trend rate for the  $ARE_{SW}$  is  $+3.6 \text{ Wm}^{-2}$  per decade (statistically significant at the 95%

466 of significance level). This decrease in the aerosol radiative effects is in line with a slight decrease  
467 in the AOD levels in the Iberian Peninsula in the last decade.

468 3) The intra-annual ARE cycle exhibits larger values during the spring and summer months when  
469 the likelihood of high aerosol loading over the Iberian Peninsula increases. In general, the annual  
470 AOD cycle is driven by the occurrence of Saharan dust events.

471 4) The AFE values at the six stations used in this study are in good agreement. Conditions of high  $\alpha$   
472 (small particles predominate) and low SSA (high absorption) lead to the largest negative AFE  
473 values. Overall, as an average for the Iberian Peninsula:  $AFE_{UV} = -6 \text{ Wm}^{-2}\tau^{-1}$ ,  $AFE_{VIS} = -34 \text{ Wm}^{-2}\tau^{-1}$ ,  
474  $AFE_{NIR} = -19 \text{ Wm}^{-2}\tau^{-1}$ , and  $AFE_{SW} = -59 \text{ Wm}^{-2}\tau^{-1}$ .

475 5) The contribution of the ultraviolet, visible, and infrared to total shortwave aerosol forcing  
476 efficiency is governed by the aerosol type. In general, the visible part of the spectrum is the most  
477 dominant part. Non-absorbing large particles cause a more equal contribution of VIS and NIR  
478 intervals, while the UV range shows a higher contribution for absorbing fine particles.

479

480

## 481 **Appendix A**

482 The two choices in the performance of radiative transfer simulations from the libRadtran code  
483 concerning aerosol properties are justified in this section.

484 First at all, as it is mentioned in the text, most of the data present  $AOD_{440nm} < 0.15$  (~70% for  
485 Palencia, Granada, and Évora sites). For these low values,  $SSA = 0.9$  and  $g = 0.75$  are selected by  
486 the representativeness of the local aerosols in the six sites of study (e.g., Cachorro et al., 2010). To  
487 analyze possible uncertainties emerging from this choice, the radiative net fluxes are also evaluated

488 for SSA and  $g$  values covering the most variety of aerosols observed in the Iberian Peninsula.  
489 Hence,  $SSA_1 = 0.8$ ,  $SSA_2 = 1.0$ ,  $g_1 = 0.65$ , and  $g_2 = 0.80$  are selected in this analysis. Four  
490 possibilities or scenarios are simulated mixing the two values of the aerosol properties. The  
491 radiation obtained in each scenario is compared with the assumed case of  $SSA = 0.9$  and  $g = 0.75$ .  
492 The two optical properties are also fixed as non-wavelength-dependent in this analysis. The  
493  $AOD_{440nm}$  used is 0.15, the worst scenario possible for these cases because the higher the AOD the  
494 stronger the impact of aerosol properties. The simulations are performed for the four spectral  
495 ranges. Table A1 shows the mean relative difference observed for the four scenarios and two  
496 different SZAs ( $30^\circ$  and  $60^\circ$ ). The assumption considered in this study causes, in the worst possible  
497 scenarios, errors in the ARE retrievals (obtained as the expanded errors from the radiative  
498 uncertainty)  $< 10\%$ ,  $< 6\%$ ,  $< 3\%$ , and  $< 5\%$  for the UV, VIS, NIR, and SW ranges, respectively. As  
499 the cases with  $AOD_{440nm} < 0.15$  are the large majority of the Iberian Peninsula, they should be  
500 included in the study. The experimental retrievals of SSA and  $g$  for these cases with low AOD  
501 present large uncertainties, and no reliable information can be used to verify our assumption.  
502 Hence, the results of this sensitivity study are adequate. As the SSA influences the diffuse radiation,  
503 the worst results are obtained at large SZAs. The impact of  $g$  on the net fluxes is very weak. In  
504 conclusion, the choice of  $SSA = 0.9$  and  $g = 0.75$  in a clean scenario ( $AOD_{440nm} < 0.15$ ) is proven as  
505 adequate because of two reasons: a) representativeness of the local aerosols which can be mixture  
506 of different types, and b) the low uncertainty produced in the simulations by SSA and  $g$  under these  
507 conditions.

508 The choice of fixed SSA and  $g$  values within each of the spectral ranges (UV, VIS, and NIR)  
509 represented by the CIMEL spectral measurements is also justified here. The aerosol models by  
510 Shettle (1989) included in the libRadtran code (see Mayer and Kylling, 2005) are used to evaluate  
511 the uncertainty of using this approximation. The continental clean aerosols (most common type in  
512 the Iberian Peninsula, see Figure 3), and continental polluted aerosols (also very common, which

513 present an extreme case of absorption) are tested in this analysis. The simulations are performed for  
514 the expected spectral behavior of SSA and  $g$  following Shettle (1989) and the case of fixed  
515 properties in the UV (SSA and  $g$  values at 440 nm), VIS (SSA and  $g$  values at 675 nm), and NIR  
516 intervals (SSA and  $g$  average of values at 870 and 1020 nm). Figure A1 presents the evolution of  
517 the relative error (considering as reference the net flux with the expected spectral dependence of  
518 aerosol properties) for several AOD values between aerosol-free and  $\text{AOD}_{550\text{nm}} = 0.6$ . In the case of  
519 continental clean aerosols (Figure A1.a), the error of using our assumption is lower than 5% for all  
520 SZAs and spectral ranges. Therefore, as the large majority of aerosol particles are of this type, the  
521 methodology used and proposed in this study only introduces a relative error below 5% in the  
522 majority of the simulations. With respect to the continental polluted aerosols (Figure A1.b), the  
523 error increases achieving a maximum around 20% for the UV range and very turbid conditions. For  
524 large AOD conditions in the Iberian Peninsula (e.g.,  $\text{AOD}_{550\text{nm}} = 0.4$ ) but with low frequency of  
525 occurrence in contrast to  $\text{AOD}_{440\text{nm}} < 0.15$ , the error of the SW range is below 5%. However, the  
526 UV range is more sensitive to our method and the error is around 15% at  $\text{SZA} = 60^\circ$ . As it was  
527 mentioned above, the errors are larger for large SZAs because of the possible interaction between  
528 absorption and scattering processes resulting the diffuse radiation. The visible range is more  
529 sensitive to the spectral variations than the NIR interval, which exhibits a maximum error around  
530 11% at  $\text{SZA} = 60^\circ$  and  $\text{AOD}_{550\text{nm}} = 0.6$ . The daily net radiative fluxes are also evaluated for the two  
531 aerosol types in order to quantify the uncertainty in the final simulated data used in this study. For  
532 Palencia site (and the corresponding SZA evolution), a daily value for the June 20th is simulated  
533 assuming  $\text{TOC} = 300$  DU and  $\text{PWC} = 1$  cm. The results for the continental polluted case with  
534  $\text{AOD}_{440\text{nm}} = 0.4$  exhibit differences between the spectral and fixed-band aerosol properties of: 7.5%,  
535 5.3%, 4.0%, and 4.8% for the UV, VIS, NIR, and SW intervals. The relative errors for the same  
536 intervals with continental clean (and same AOD value) are: 1.9%, 1.2%, 1.4%, and 1.4%,  
537 respectively. Therefore, the uncertainty due to fixed optical properties in each spectral range is

538 dependent on the aerosol type but the error caused can be considered as acceptable. Since actual  
539 aerosols often present mixtures of different types, the uncertainty of using the theoretical spectral  
540 evolution for one type (given by an aerosol model) can also produce uncertainties which should be  
541 taken into account. Although other aerosol types are not tested in this analysis, a similar behavior  
542 can be expected. For instance, for the case of desert dust aerosols, Román et al. (2013) found a  
543 slight influence of spectral aerosol absorption properties on UV irradiance analyzing a strong  
544 Saharan intrusion over Granada site.

545 Therefore, the two assumptions performed in this study in the simulations are adequate for the  
546 evaluation of net fluxes and aerosol radiative effects. The uncertainties that can be introduced in the  
547 daily values are acceptable being around or smaller than 5% for the net SW radiation. This  
548 uncertainty is usually achieved in clear-sky modeling (e.g., Mateos et al., 2013a).

549

## 550 **Acknowledgments**

551 The work is supported by the Spanish Ministry of Science and Technology (currently MINECO)  
552 through projects CGL2010-18782, CSD2007-00067, CGL2011-29921-C02-01, CGL2011-23413,  
553 CGL2011-24891, CGL2011-13085-E, CGL2011-13580-E, CGL2012-33576, and CGL2012-  
554 33576; FEDER (Programa Operacional Factores de Competitividade - COMPETE). Also by  
555 Portuguese funding through FCT - Fundação para a Ciência e a Tecnologia in the framework of  
556 project FCOMP-01-0124-FEDER-009303 (PTDC / CTE-ATM / 102142 / 2008); the Évora  
557 Geophysics Centre, Portugal, under the contract with FCT, PEst-OE/CTE/UI0078/2014; and the  
558 Andalusia Regional Government through projects P08- RNM-3568 and P10-RNM-6299. The  
559 research leading to these results has received also funding from the European Union Seventh  
560 Framework Programme (FP7/2007-2013) under grant agreement Nr. 262254 [ACTRIS]. Manuel  
561 Antón and Carlos Toledano thank Ministerio de Ciencia e Innovación and Fondo Social Europeo



562 for the awards of a postdoctoral grant (Ramón y Cajal), and Mar Sorribas for postdoctoral grant  
563 (Juan de la Cierva). We must specially thank the AERONET-GSFC, PHOTONS-LOA and RIMA-  
564 GOA-UVa staff for their scientific and technical support. Ozone Monitoring Instrument (OMI) and  
565 Total Ozone Mapping Spectrometer (TOMS) ozone column data were obtained from the Giovanni  
566 online data system, developed and maintained by the NASA GES DISC.

567

## 568 **References**

569 Aas, W., Espen Yttri, K., Stohl, A., Lund Myhre, C., Karl, M., Tsyro, S., Marečková, K.,  
570 Wankmüller, R., Klimont, Z., Heyes, C., Alastuey, A., Querol, X., Pérez, N., Moreno, T.,  
571 Lucarelli, F., Areskoug, H., Balan, V., Cavalli, F., Putaud, J.P., Cape J.N., Catrambone, M.,  
572 Ceburnis, D., Conil, S., Gevorgyan, L., Jaffrezo, J.L., Hueglin, C., Mihalopoulos, N.,  
573 Mitosinkova, M., Riffault, V., Sellegri, K., Spindler, G., Schuck, T., Pfeffer, U., Breuer, L.,  
574 Adolfs, D., Chuntanova, L., Arabidze, M., and Abdulazizov, E.: Transboundary particulate  
575 matter in Europe Status report 2013, EMEP Report, 4/2013 (Ref. O-7726), ISSN: 1504-6109  
576 (print), 1504-6192 (online), 2013.

577 Antón, M., Gil, J.E., Fernández-Gálvez, J., Lyamani, H., Valenzuela, A., Foyo-Moreno, I., Olmo, F.  
578 J., and Alados-Arboledas, L.: Evaluation of the aerosol forcing efficiency in the UV erythemat  
579 range at Granada, Spain, *J. Geophys. Res.*, 116, D20214, doi:10.1029/2011JD016112, 2011.

580 Antón, M., Valenzuela, A., Cazorla, A., Gil, J.E., Fernández-Gálvez, J., Lyamani, H., Foyo-  
581 Moreno, I., Olmo, F.J., Alados-Arboledas, L.: Global and diffuse shortwave irradiance during a  
582 strong desert dust episode at Granada (Spain), *Atmos. Res.*, 118, 232–239,  
583 doi:10.1016/j.atmosres.2012.07.007, 2012.

584 Antón, M., Valenzuela, A., Mateos, D., Alados, I., Foyo-Moreno, I., Olmo, F.J., Alados-Arboledas,  
585 L.: Lonwave aerosol radiative effects during an extreme desert dust event in Southeastern  
586 Spain, *Atmos. Res.*, doi: 10.1016/j.atmosres.2014.05.022, 2014.

587 Barja, B., and Antuña, J.C.: The effect of optically thin cirrus clouds on solar radiation in  
588 Camagüey Cuba. *Atmos. Chem. Phys.*, 11, 8625–8634, doi:10.5194/acp-11-8625-2011, 2011.

589 Barmpadimos, I., Keller, J., Oderbolz, D., Hueglin C., and Prévôt, A.S.H.: One decade of parallel  
590 fine (PM<sub>2.5</sub>) and coarse (PM<sub>10</sub>- PM<sub>2.5</sub>) particulate matter measurements in Europe: trends and  
591 variability, *Atmos. Chem. Phys.* 12, 3189-3203, doi: 10.5194/acp-12.3189-2012, 2012.

592 Bennouna, Y., Cachorro, V., Toledano, C., Berjón, A., Prats, N., Fuertes, D., Gonzalez, R.,  
593 Rodrigo, R., Torres, B., and de Frutos, A.: Comparison of atmospheric aerosol climatologies  
594 over southwestern Spain derived from AERONET and MODIS, *Rem. Sen. Env.* 115, 1272-  
595 1284, 2011.

596 Bennouna, Y.S., Cachorro, V., Burgos, M.A., Toledano, C., Torres, B., and de Frutos, A.:  
597 Relationships between columnar aerosol optical properties and surface Particulate Matter  
598 observations in north-central Spain from long-term records (2003-2011), *Atmos. Meas. Tech.*  
599 *Discuss.*, 7, 5829-5882, doi:10.5194/amtd-7-5829-2014, 2014.

600 Boucher, O., Randall, D., Artaxo, P., Bretherton, C., Feingold, G., Forster, P., Kerminen, V.-M.,  
601 Kondo, Y., Liao, H., Lohmann, U., Rasch, P., Satheesh, S.K., Sherwood, S., Stevens, B., and  
602 Zhang, X.Y.: Clouds and aerosols. In *Climate Change 2013: The Physical Science Basis.*  
603 *Contribution of Working Group I to the Fifth Assessment Report of the Intergovernmental*  
604 *Panel on Climate Change.* T.F. Stocker, D. Qin, G.-K. Plattner, M. Tignor, S.K. Allen, J.  
605 Doschung, A. Nauels, Y. Xia, V. Bex, and P.M. Midgley, Eds. Cambridge University Press,  
606 571-657, 2013.

607 Bush, B. C., and Valero, F. P. J.: Surface aerosol radiative forcing at Gosan during the ACE– Asia  
608 campaign, *J. Geophys. Res.*, 108(D23), 8660, doi:10.1029/2002JD003233, 2003.

609 Cachorro, V. E., Toledano, C., Prats, N., Sorribas, M., Mogo, S., Berjón, A., Torres, B., Rodrigo,  
610 R., de la Rosa, J., and De Frutos, A. M.: The strongest desert dust intrusion mixed with smoke  
611 over the Iberian Peninsula registered with Sun photometry, *J. Geophys. Res.*, 113, D14S04,  
612 doi:10.1029/2007JD009582, 2008.

613 Cachorro, V. E., Toledano, C., Antón, M., Berjón, A., de Frutos, A., Vilaplana, J. M., Arola, A., and  
614 Krotkov, N. A.: Comparison of UV irradiances from Aura/Ozone Monitoring Instrument  
615 (OMI) with Brewer measurements at El Arenosillo (Spain) – Part 2: Analysis of site aerosol  
616 influence, *Atmos. Chem. Phys.*, 10, 11867-11880, doi:10.5194/acp-10-11867-2010, 2010.

617 Collaud Coen, M., Andrews, E., Asmi, A., Baltensperger, U., Bukowiecki, N., Day, D., Fiebig, M.,  
618 Fjaeraa, A. M., Flentje, H., Hyvärinen, A., Jefferson, A., Jennings, S. G., Kouvarakis, G.,  
619 Lihavainen, H., Lund Myhre, C., Malm, W. C., Mihapopoulos, N., Molnar, J. V., O'Dowd, C.,  
620 Ogren, J. A., Schichtel, B. A., Sheridan, P., Virkkula, A., Weingartner, E., Weller, R., and  
621 Laj, P.: Aerosol decadal trends – Part 1: In-situ optical measurements at GAW and IMPROVE  
622 stations, *Atmos. Chem. Phys.*, 13, 869-894, doi:10.5194/acp-13-869-2013, 2013.

623 Córdoba-Jabonero, C., Sorribas, M., Guerrero-Rascado, J.L., Adame, J.A., Hernández, Y.,  
624 Lyamani, H., Cachorro, V., Gil, M., Alados-Arboledas, L., Cuevas, E., and de la Morena, B.:  
625 Synergetic monitoring of Saharan dust plumes and potential impact on surface: a case study of  
626 dust transport from Canary Islands to Iberian Peninsula, *Atmos. Chem. Phys.*, 11, 3067-3091,  
627 doi:10.5194/acp-11-3067-2011, 2011.

628 Costa, M. J., Levizzani, V., and Silva, A. M.: Aerosol Characterization and Direct Radiative  
629 Forcing Assessment over the Ocean. Part II: Application to Test Cases and Validation. *J. Appl.*  
630 *Meteor.*, 43, 1818–1833, doi: <http://dx.doi.org/10.1175/JAM2157.1>, 2004.

631 Costa, M.J., Sohn, B.J., Levizzani, V., and Silva, A.M.: Radiative forcing of Asian dust determined  
632 from the synergized GOME and GMS satellite data - A case study, *J. Meteorol. Soc. Jpn.*,  
633 84(1), 85-95, doi: 10.2151/jmsj.84.85, 2006.

634 Cusack, M., Alastuey, A., Pérez, N., Pey, J., and Querol, X.: Trends of particulate matter (PM<sub>2.5</sub>)  
635 and chemical composition at a regional site in the Western Mediterranean over the last nine  
636 years (2002-2010), *Atmos. Env.* 12, 8341-8357, doi: 10.5194/acp-12-8341-2012, 2012.

637 de Miguel, A., Mateos, D., Bilbao, J., and Román, R.: Sensitivity analysis of ratio between  
638 ultraviolet and total shortwave solar radiation to cloudiness, ozone, aerosols and precipitable  
639 water, *Atmos. Res.*, 102, 136–144, doi:10.1016/j.atmosres.2011.06.019., 2011.

640 Di Biagio, C., di Sarra, A., Meloni, D., Monteleone, F., Piacentino, S., and Sferlazzo, D.:  
641 Measurements of Mediterranean aerosol radiative forcing and influence of the single scattering  
642 albedo, *J. Geophys. Res.*, 114, D06211, doi:10.1029/2008JD011037, 2009.

643 Di Biagio, C., di Sarra, A., and Meloni, D.: Large atmospheric shortwave radiative forcing by  
644 Mediterranean aerosols derived from simultaneous ground-based and spaceborne observations  
645 and dependence on the aerosol type and single scattering albedo, *J. Geophys. Res.*, 115,  
646 D10209, doi:10.1029/2009JD012697, 2010.

647 di Sarra, A., Pace, G, Meloni, D., De Silvestri, L., Piacentino, S., and Monteleone, F.: Surface  
648 shortwave radiative forcing of different aerosol types in the Mediterranean, *Geophys. Res.*  
649 *Lett.*, 35, L02714, doi:10.1029/2007GL032395, 2008.

650 di Sarra, A., Di Biagio, C., Meloni, D., Monteleone, F., Pace, G., Pugnaghi, S., and Sferlazzo, D.:  
651 Shortwave and longwave radiative effects of the intense Saharan dust event of 25–26 March  
652 2010 at Lampedusa (Mediterranean Sea), *J. Geophys. Res.*, 116, D23209,  
653 doi:10.1029/2011JD016238, 2011.

654 Díaz, A. M., García, O.E., Díaz, J.P., Expósito, F.J., Utrillas, M.P., Martínez-Lozano, J.A., Alados-  
655 Arboledas, L., Olmo, F.J., Lorente, J., Cachorro, V., Horvath, H., Labajo, A., Sorribas, M.,  
656 Vilaplana, J.M., Silva, A.M., Elias, T., Pujadas, M., Rodrigues, J.A., and González, J.A.:  
657 Aerosol radiative forcing efficiency in the UV region over southeastern Mediterranean:  
658 VELETA2002 campaign, *J. Geophys. Res.*, 112, D06213, doi:10.1029/2006JD007348, 2007.

659 Dubovik, O., and King, M.D.: A flexible inversion algorithm for retrieval of aerosol optical  
660 properties from Sun and sky radiance measurements, *J. Geophys. Res.*, 105, 20673-20696,  
661 2000.

662 Dubovik, O., Smirnov, A., Holben, B.N., King, M.D., Kaufman, Y.J., Eck, T.F., and Slutsker, I.:  
663 Accuracy assessments of aerosol optical properties retrieved from Aerosol Robotic Network  
664 (AERONET) Sun and sky radiance measurements, *J. Geophys. Res.*, 105, 9791-9806, 2000.

665 Dubovik, O., Sinyuk, A., Lapyonok, T., Holben, B.N., Mishchenko, M., Yang, P., Eck, T.F.,  
666 Volten, H., Muñoz, O., Veihelmann, B., van der Zande, W.J., Leon, J.F., Sorokin, M., and  
667 Slutsker, I.: Application of spheroid models to account for aerosol particle nonsphericity in  
668 remote sensing of desert dust, *J. Geophys. Res.*, 111, D11208, 2006.

669 Esteve, A.R., Estellés, V., Utrillas, M.P., and Martínez-Lozano, J.A.: Analysis of the aerosol  
670 radiative forcing over a Mediterranean urban coastal site, *Atmos. Res.*, 137, 194-204,  
671 <http://dx.doi.org/10.1016/j.atmosres.2013.10.009>, 2014.

672 Foyo-Moreno, I., Alados, I., Antón, M., Fernández-Gálvez, J., Cazorla, A., and Alados-Arboledas,  
673 L.: Estimating aerosol characteristics from solar irradiance measurements at an urban location  
674 in Southeastern Spain, *J. Geophys. Res. Atmos.*, 119, 1845–1859, doi:10.1002/2013JD020599,  
675 2014.

676 García, O. E., Díaz, A. M., and Expósito, F. J.: Validation of AERONET estimates of atmospheric  
677 solar fluxes and aerosol radiative forcing by ground-based broadband measurements, *J.*  
678 *Geophys. Res.*, 113, D21207, doi:10.1029/2008JD010211, 2008.

679 García, R.D., García, O.E., Cuevas, E., Cachorro, V.E., Romero-Campos, P.M., Ramos, R., and de  
680 Frutos, A.M.: Solar radiation measurements compared to simulations at the BSRN Izaña  
681 station: Mineral dust radiative forcing and efficiency study, *J. Geophys. Res. Atmos.*, 119, 179–  
682 194, doi:10.1002/2013JD020301, 2014.

683 Gkikas, A., Hatzianastassiou, N., Mihalopoulos, N., Katsoulis, V., Kazadzis, S., Pey, J., Querol, X.,  
684 and Torres, O.: The regime of intense desert dust episodes in the Mediterranean based on  
685 contemporary satellite observations and ground measurements, *Atmos. Chem. Phys.*, 13,  
686 12135-12154, doi:10.5194/acp-13-12135-2013, 2013.

687 Guerrero-Rascado, J.L., Olmo, F. J., Avilés-Rodríguez, I., Navas-Guzmán, F., Pérez-Ramírez, D.,  
688 Lyamani, H., and Alados-Arboledas, L.: Extreme Saharan dust event over the southern Iberian  
689 Peninsula in September 2007: active and passive remote sensing from surface and Satellite,  
690 *Atmos. Chem. Phys.*, 9, 8453–8469, doi:10.5194/acp-9-8453-2009, 2009.

691 Gueymard, C.: The sun's total and spectral irradiance for solar energy applications and solar  
692 radiation models, *Sol. Energy*, 76, 423-453, 2004.

693 Hansen, J. E., Sato, M., Lacis, A., Ruedy, R., Tegen, I., and Matthews, E.: Climate forcings in the  
694 industrial era, *Proc. Natl. Acad. Sci. U.S.A.*, 95, 12753–12758, doi:10.1073/pnas.95.22.12753,  
695 1998.

696 Hatzianastassiou, N., Katsoulis, B., and Vardavas, I.: Global distribution of aerosol direct radiative  
697 forcing in the ultraviolet and visible arising under clear skies, *Tellus B*, 56, 51–71,  
698 doi:10.1111/j.1600-0889.2004.00085.x, 2004.

699 Hess, M., Koepke, P., and Schult, I.: Optical Properties of Aerosols and Clouds: The Software  
700 Package OPAC, *Bull. Am. Meteorol. Soc.*, 79, 831-844, 1998.

701 Holben, B.N., Eck, T.F., Slutsker, I., Tanré, D., Buis, J.P., Setzer, A., Vermote, E., Reagan, J.A.,  
702 KAufman, Y.J., Nakajima, T., Lavenu, F., Jankowiak, I., and Smirnov, A.: AERONET – A  
703 federated instrument network and data archive for aerosol characterization, *Rem. Sen. Environ.*,  
704 66, 1–16, 1998.

705 Horvath, H., Alados Arboledas, L., Olmo, F. J., Jovanovic, O., Gangl, M., Kaller, W., Sánchez, C.,  
706 Sauerzopf, H., and Seidl, S.: Optical characteristics of the aerosol in Spain and Austria and its  
707 effect on radiative forcing, *J. Geophys. Res.*, 107(D19), 4386, doi:10.1029/2001JD001472,  
708 2002.

709 Jayaraman, A., Lubin, D., Ramachandran, S., Ramanathan, V. , Woodbridge, E., Collins, W. D.,  
710 and Zalpuri, K. S.: Direct observations of aerosol radiative forcing over the tropical Indian  
711 Ocean during the January–February 1996 pre-INDOEX cruise, *J. Geophys. Res.*, 103, 13,827–  
712 13,836, doi:10.1029/98JD00559, 1998.

713 Kazadzis, S., Kouremeti, N., Bais, A., Kazantzidis, A., and Meleti, C.: Aerosol forcing efficiency in  
714 the UVA region from spectral solar irradiance measurements at an urban environment, *Ann.*  
715 *Geophys.*, 27, 2515–2522, doi:10.5194/angeo-27-2515-2009, 2009.

716 Lucht, W. and Roujean, J.L.: Consideration in parametric modelling of BRDF and albedo from  
717 multi-angular satellite sensors observations, *Remote Sens. Rev.*, 18, 343–379, 2000.

718 Lyamani, H., Olmo, F.J., and Alados-Arboledas, L.: Saharan dust outbreak over southeastern Spain  
719 as detected by sun photometer, *Atmos. Env.*, 39, 7276-7284,  
720 doi:10.1016/j.atmosenv.2005.09.011, 2005.

721 Lyamani, H., Olmo, F. J., Alcántara, A., and Alados-Arboledas, L.: Atmospheric aerosols during  
722 the 2003 heat wave in southeastern Spain II: Microphysical columnar properties and radiative  
723 forcing, *Atmos. Environ.*, 40, 6465–6476, doi:10.1016/j.atmosenv.2006.04.047, 2006.

724 Mallet, M., Dubovik, O., Nabat, P., Dulac, F., Kahn, R., Sciare, J., Paronis, D., and Leon, J.F.:  
725 Absorption properties of Mediterranean aerosols obtained from multi-year ground-based  
726 remote sensing observations, *Atmos. Chem. Phys.*, 13, 9195-9210, doi:10.5194/acp-13-9195-  
727 2013, 2013.

728 Mateos, D., Antón, M., Valenzuela, A., Cazorla, A., Olmo, F.J., and Alados-Arboledas, L.: Short-  
729 wave radiative forcing at the surface for cloudy systems at a midlatitude site, *Tellus B*, 65,  
730 21069, <http://dx.doi.org/10.3402/tellusb.v65i0.21069>, 2013a.

731 Mateos, D., Antón, M., Sanchez-Lorenzo, A., Calbó, J., and Wild, M.: Long-term changes in the  
732 radiative effects of aerosols and clouds in a mid-latitude region (1985–2010), *Global Planet.*  
733 *Change*, 111, 288-295, <http://dx.doi.org/10.1016/j.gloplacha.2013.10.004>, 2013b.

734 Mateos, D., Sanchez-Lorenzo, A., Antón, M., Cachorro, V.E., Calbó, J., Costa, M.J., Torres, B., and  
735 Wild, M.: Quantifying the respective roles of aerosols and clouds in the strong brightening  
736 since the early 2000s over the Iberian Peninsula, *J. Geophys. Res. Atmos.*, 119, 10382–10393,  
737 doi:10.1002/2014JD022076, 2014.



738 Mayer, B., and Kylling, A.: Technical note: The libRadtran software package for radiative transfer  
739 calculations – description and examples of use, *Atmos. Chem.Phys.*, 5, 1855–1877, 2005.

740 Meloni, D., di Sarra, A., DeLuisi, J., Di Iorio, T., Fiocco, G., Junkerman, W., and Pace, G.:  
741 Tropospheric aerosols in the Mediterranean: 2. Radiative effects through model simulations and  
742 measurements, *J. Geophys. Res.*, 108(D10), 4317, doi:10.1029/2002JD002807, 2003.

743 Meloni, D., di Sarra, A., Di Iorio, T., and Fiocco, G.: Influence of the vertical profile of Saharan  
744 dust on the visible direct radiative forcing, *J. Quant. Spectrosc. Radiat. Transfer*, 93, 397–413,  
745 2005.

746 Moody, E.G., King, M.D., Platnick, S., Schaaf, C.B., and Gao, F.: Spatially complete global  
747 spectral surface albedos: value-added datasets derived from Terra MODIS land products, *IEEE*  
748 *T. Geosci. Remote.*, 43, 144–158, 2005.

749 Navas-Guzmán, F., Bravo-Aranda, J.A., Guerrero-Rascado, J.L., Granados-Muñoz, M.J., and  
750 Alados-Arboledas, L.: Statistical analysis of aerosol optical properties retrieved by Raman lidar  
751 over Southeastern Spain, *Tellus B*, 65, 21234, <http://dx.doi.org/10.3402/tellusb.v65i0.21234>,  
752 2013.

753 Nikitidou, E., Kazantzidis, A., De Bock, V., and De Backer, H.: The aerosol forcing efficiency in  
754 the UV region and the estimation of single scattering albedo at a typical West European site,  
755 *Atmos. Env.*, 69, 313-320, doi:<http://dx.doi.org/10.1016/j.atmosenv.2012.12.035>, 2013.

756 Obregón M.A., Pereira S, Wagner F, Serrano A, Cancillo ML, Silva AM.: Regional differences of  
757 column aerosol parameters in western Iberian Península, *Atmos. Environ.*, 62, 208-219, doi:  
758 [10.1016/j.atmosenv.2012.08.016](http://dx.doi.org/10.1016/j.atmosenv.2012.08.016), 2012

759 Pace, G., di Sarra, A., Meloni, D., Piacentino, S., and Chamard, P.: Aerosol optical properties at  
760 Lampedusa (central Mediterranean): 1. Influence of transport and identification of different  
761 aerosol types, *Atmos. Chem. Phys.*, 6, 697–713, 2006.

762 Panicker, A. S., Pandithurai, G., Safai, P. D., and Kewat, S.: Observations of enhanced aerosol  
763 longwave radiative forcing over an urban environment, *Geophys. Res. Lett.*, 35, L04817,  
764 doi:10.1029/2007GL032879, 2008.

765 Pérez-Ramírez, D., Aceituno, J., Ruiz, B., Olmo, F.J., and Alados-Arboledas, L.: Development and  
766 calibration of a star photometer to measure the aerosol optical depth: Smoke observations at a  
767 high mountain site, *Atmos. Env.* 42(11), 2733–2738, 2008.

768 Pey, J., Querol, X., Alastuey, A., Forastiere, F., and Stafoggia, M. African dust outbreaks over the  
769 Mediterranean Basin during 2001–2011: PM<sub>10</sub> concentrations, phenomenology and trends, and  
770 its relation with synoptic and mesoscale meteorology, *Atmos. Chem. Phys.*, 13, 1395–1410,  
771 doi:10.5194/acp-13-1395-2013, 2013.

772 Prats, N., Cachorro, V.E., Berjón, A., Toledano, C., and De Frutos, A.M.: Column-integrated  
773 aerosol microphysical properties from AERONET Sun photometer over south-western Spain.  
774 *Atmos. Chem. Phys.* 11, 12353–12547, doi:10.5194/acpd-11-12353-2011, 2011.

775 Querol, X., Alastuey, A., Pandolfi, M., Reche, C., Pérez, N., Minguillón, M.C., Moreno, T., Viana,  
776 M., Escudero, M., Orío, A., Pallarés, M., and Reina, F.: 2001–2012 trends of air quality in  
777 Spain, *Sci. Total Environ.*, 490, 957–969, 2014.

778 Rajeev, K., and Ramanathan, V.: Direct observations of clear-sky aerosol radiative forcing from  
779 space during the Indian Ocean Experiment, *J. Geophys. Res.*, 106, 17,221–17,235,  
780 doi:10.1029/2000JD900723, 2001.

781 Reche, C., Viana, M., Moreno, T., Querol, X., Alastuey, A., Pey, J., Pandolfi, M., Prévôt, A., Mohr,  
782 C., Richard, A., Artiñano, B., Gomez-Moreno, F.J., and Cots, N.: Peculiarities in atmospheric  
783 particle number and size-resolved speciation in an urban area in the western Mediterranean:  
784 Results from the DAURE campaign, *Atmos. Env.*, 45, 5282-5293,  
785 doi:10.1016/j.atmosenv.2011.06.059, 2011.

786 Román, R., Antón, M., Valenzuela, A., Gil, J.E., Lyamani, H., de Miguel, A., Olmo, F.J., Bilbao, J.,  
787 and Alados-Arboledas, L.: Evaluation of the desert dust effects on global, direct, and diffuse  
788 spectral ultraviolet irradiance, *Tellus B*, 65, 19578,  
789 <http://dx.doi.org/10.3402/tellusb.v65i0.19578>, 2013.

790 Román, R., Bilbao, J., and de Miguel, A.: Solar radiation simulations in the Iberian Peninsula:  
791 Accuracy and sensitivity to uncertainties in inputs of a radiative transfer model, *J. Quant.*  
792 *Spectrosc. Ra.*, 145, 95-109, 2014.

793 Ruckstuhl, C., Philipona, R., Behrens, K., Coen M.C., Dürr, B., Heimo, A., Mätzler, C., Nyeki, S.,  
794 Ohmura, A., Vuilleumier, L., Weller, M., Wehrl, C., and Zelenka, A.: Aerosol and cloud  
795 effects on solar brightening and the recent rapid warming, *Geophys. Res. Lett.*, 35, L12708,  
796 doi:10.1029/2008GL034228, 2008.

797 Saha, A., Mallet, M., Roger, J. C., Dubuisson, P., Piazzola, J., and Despiiau, S.: One year  
798 measurements of aerosol optical properties over an urban coastal site: Effect on local direct  
799 radiative forcing, *Atmos. Res.*, 90, 195–202, doi:10.1016/j.atmosres.2008.02.003, 2008.

800 Sanchez-Lorenzo, A., Calbó, J., and Wild, M.: Global and diffuse solar radiation in Spain: Building  
801 a homogeneous dataset and assessing trends, *Global Planet. Change*, 100, 343-352,  
802 <http://dx.doi.org/10.1016/j.gloplacha.2012.11.010>, 2013.

803 Santos, D., Costa, M. J., and Silva, A. M.: Direct SW aerosol radiative forcing over Portugal,  
804 Atmos. Chem. Phys., 8, 5771–5786, doi:10.5194/acp-8-5771-2008, 2008.

805 Schuster, G. L., Dubovik, O., and Holben, B. N.: Angstrom exponent and bimodal aerosol size  
806 distributions, J. Geophys. Res., 111, D07207, doi:10.1029/2005JD006328, 2006.

807 Sen, P. K.: Estimates of the regression coefficient based on Kendall's tau, J. Am., Stat. Assoc., 63,  
808 1379–1389, 1968.

809 Shettle, E. P.: Models of aerosols, clouds and precipitation for atmospheric propagation studies,  
810 paper presented at Conference on Atmospheric Propagation in the UV, Visible, IR and MM-  
811 Region and Related System Aspects, NATO Adv. Group for Aerosp. Res. and Dev.,  
812 Copenhagen, 1989.

813 Stamnes, K., Tsay, S.C., Wiscombe, W., and Laszlo, I.: DISORT, a General-Purpose Fortran  
814 Program for Discrete-Ordinate-Method Radiative Transfer in Scattering and Emitting Layered  
815 Media: Documentation of Methodology, Tech. rep. Dept. of Physics and Engineering Physics,  
816 Stevens Institute of Technology, Hoboken, NJ 07030, 2000.

817 Steinbrecht, W., Köhler, U., Claude, H., Weber, M., Burrows, J.P., and van der A, R.J.: Very high  
818 ozone columns at northern mid-latitudes in 2010, Geophys Res Lett, 38, L06803,  
819 doi:10.1029/2010GL046634, 2011.

820 Toledano, C., Cachorro, V.E., Berjon, A., de Frutos, A.M., Sorribas, M., de la Morena, B., and  
821 Goloub, P.: Aerosol optical depth and Ångström exponent climatology at El Arenosillo  
822 AERONET site (Huelva, Spain), Q. J. R. Meteorol. Soc., 133, 795-807, 2007a.

823 Toledano, C., Cachorro, V.E., de Frutos, A.M., Sorribas, M., Prats, N., and de la Morena, B.:  
824 Inventory of African desert dust events over the southwestern Iberian Peninsula in 2000-2005

825 with an AERONET Cimel Sun photometer, *J. Geophys. Res.* 112, doi:10.1029/2006JD008307,  
826 2007b.

827 Valenzuela, A., Olmo, F.J., Lyamani, H., Antón, M., Quirantes, A., and Alados-Arboledas, L.:  
828 Aerosol radiative forcing during African desert dust events (2005-2010) over Southeastern  
829 Spain, *Atmos. Chem. Phys.* 12, 10331–10351, doi:10.5194/acp-12-10331-2012, 2012.

830 Zhou, M., Yu, H., Dickinson, R. E., Dubovik, O., and Holben, B. N.: A normalized description of  
831 the direct effect of key aerosol types on solar radiation as estimated from Aerosol Robotic  
832 Network aerosols and Moderate Resolution Imaging Spectroradiometer albedos, *J. Geophys.*  
833 *Res.*, 110, D19202, doi:10.1029/2005JD005909, 2005.

834

837 **Table 1.** Coordinates and time interval of the six AERONET sites used in this study.

Station	Latitude (°N)	Longitude (°E)	Altitude a.s.l. (m)	Time interval
Palencia	41.99	-4.52	750	2003-2012
Barcelona	41.39	2.12	125	2004-2012
Cabo da Roca	38.78	-9.50	140	2003-2011
Évora	38.57	-7.91	293	2005-2012
Granada	37.16	-3.61	680	2004-2012
El Arenosillo	37.11	-6.73	0	2000-2009

842 **Table 2.** Summary of AERONET data used for ARE calculations: aerosol optical depth (AOD),  
843 single scattering albedo (SSA), asymmetry factor (g), precipitable water vapor column (PWC).  
844 Estimated absolute uncertainty of AOD and SSA is given according to Dubovik et al. (2002), and  
845 PWC error from Holben et al. (1998).

	AERONET database	Estimated uncertainty
AOD	Level 2.0	$\pm 0.01-0.02$
SSA, g (AOD <sub>440</sub> >0.4)	Level 2.0	$\pm 0.03$ (in SSA)
SSA, g (0.15<AOD <sub>440</sub> <0.4)	Level 1.5-filtered*	$\pm 0.05-0.07$ (in SSA)
SSA, g (AOD <sub>440</sub> <0.15)	Fixed value	
PWC	Level 2.0	10-15%

846 \*Filters applied are the same as in level 2.0 except for AOD<sub>440</sub> (see text).

851 **Table 3.** AFE values and their standard error for the UV, VIS, NIR, and SW ranges for, separately,  
852 four SSA and three  $\alpha$  intervals over the Iberian Peninsula. Units are  $\text{Wm}^{-2}\tau^{-1}$ . SSA groups:  $0.85 \geq$   
853  $\text{SSA}_1 > 0.80$  (group 1),  $0.90 \geq \text{SSA}_2 > 0.85$  (group 2),  $0.95 \geq \text{SSA}_3 > 0.90$  (group 3), and  $1.0 \geq$   
854  $\text{SSA}_4 > 0.95$  (group 4); and  $\alpha$  groups:  $0 \leq \alpha_1 \leq 1$  (group 1),  $1.0 \leq \alpha_2 \leq 1.5$  (group 2), and  $1.5 < \alpha_3 \leq 2$   
855 (group 3). The average values without any classification are also presented.  
856

Variable	Group	AFE <sub>UV</sub>	AFE <sub>VIS</sub>	AFE <sub>NIR</sub>	AFE <sub>SW</sub>
$\alpha$	1	$-5.41 \pm 0.06$	$-30.1 \pm 0.3$	$-20.9 \pm 0.2$	$-56.5 \pm 0.5$
	2	$-6.60 \pm 0.09$	$-38.3 \pm 0.4$	$-19.1 \pm 0.2$	$-64.0 \pm 0.6$
	3	$-7.06 \pm 0.10$	$-39.4 \pm 0.4$	$-16.9 \pm 0.2$	$-63.3 \pm 0.7$
SSA	1	$-9.7 \pm 0.2$	$-52.8 \pm 0.8$	$-24.9 \pm 0.5$	$-87.4 \pm 1.4$
	2	$-8.19 \pm 0.10$	$-44.6 \pm 0.4$	$-21.2 \pm 0.2$	$-74.0 \pm 0.6$
	3	$-6.37 \pm 0.05$	$-35.9 \pm 0.2$	$-19.5 \pm 0.2$	$-61.8 \pm 0.3$
	4	$-4.59 \pm 0.05$	$-26.6 \pm 0.2$	$-18.1 \pm 0.2$	$-49.3 \pm 0.3$
Average		$-5.98 \pm 0.05$	$-33.7 \pm 0.2$	$-19.34 \pm 0.11$	$-59.1 \pm 0.3$

859  
860  
861

**Table 4.** Daily Forcing Efficiencies at the surface by previous studies. Legend: desert dust (DD), continental-biomass burning (C-BB), and forest fires (FF).

Reference	Aerosol Type	AFE <sub>X</sub>	Value (Wm <sup>-2</sup> τ <sup>-1</sup> )	Time period	Region	More info.
Díaz et al. (2007)	Mixed	AFE <sub>UV</sub>	-3	July 2002	Spain	290-363 nm
Meloni et al. (2005)	DD Mixed	AFE <sub>VIS</sub>	-28.4 -45.6	July 2002	Central Mediterranean	
Lyamani et al. (2006)	Mixed	AFE <sub>VIS</sub>	-75.8	August 2003	Spain	2003 heat wave
Di Biagio et al. (2010)	DD C-BB Mixed	AFE <sub>SW</sub>	-68.9 -59.0 -94.9	2004-2007	Central Mediterranean	At the equinox
Esteve et al. (2014)	Mixed	AFE <sub>SW</sub>	-139.0	2003-2011	Spain	200 cloud-free days
Santos et al. (2008)	FF	AFE <sub>SW</sub>	-113.0	2004-2005	Portugal	Absorbing aerosols
di Sarra et al. (2011)	DD	AFE <sub>SW</sub>	-55	25-26/03/2010	Central Mediterranean	Strong event
García et al. (2014)	DD	AFE <sub>SW</sub>	-59	2009-2012	Canary Islands	386 cloud-free days
Costa et al. (2006)	DD	AFE <sub>SW</sub>	-116.9	7/04/2000	Korea	SSA = 0.76
Zhou et al. (2005)	DD	AFE <sub>SW</sub>	-80/-48	Monthly aerosol climatology	North Africa and Arabian Peninsula	Depending on surface albedo
Saha et al. (2008)	C-BB Mixed	AFE <sub>SW</sub>	-97.6 -81.5	2005-2006	French Mediterranean	0.7 < SSA < 0.8
Valenzuela et al. (2012)	DD	AFE <sub>SW</sub>	-70	2005-2010	Spain	

862  
863  
864  
865  
866  
867  
868

**Table A1.** Mean relative difference (RD) in the UV, VIS, NIR, and SW net fluxes if SSA = 0.90 and g = 0.75 are compared with different SSA and g scenarios for different SZA values.

SZA	RD <sub>UV</sub> (%)	RD <sub>VIS</sub> (%)	RD <sub>NIR</sub> (%)	RD <sub>SW</sub> (%)
30	±3.4	±1.9	±0.9	±1.5
60	±4.9	±3.0	±1.5	±2.4

869  
870

871 Figure Captions

872 **Figure 1.** Annual cycle of daily values of AOD at 440 nm by box whisker plots. Triangles and  
873 horizontal solid lines indicate the monthly average and median values, respectively.

874 **Figure 2.** Annual cycle of daily values of  $\alpha$  ('alpha' in the figure) by box whisker plots. Triangles  
875 and horizontal solid lines indicate the monthly average and median values, respectively.

876 **Figure 3.** Relative frequency of aerosol type occurrence: maritime (MA), desert dust (DD),  
877 continental clean (CC), and continental polluted (CP).

878 **Figure 4.** Yearly values of AOD<sub>440nm</sub> at the six sites: Barcelona (blue diamonds), Palencia (purple  
879 triangles), Évora (red squares), Cabo da Roca (grey crosses), Granada (black stars), and El  
880 Arenosillo (green circles). The text points out the statistically significant trend obtained.

881 **Figure 5.** Evolution of yearly ARE<sub>UV</sub> (a), ARE<sub>VIS</sub> (b), ARE<sub>NIR</sub> (c), and ARE<sub>SW</sub> (d) at the six sites:  
882 Barcelona (blue diamonds), Palencia (purple triangles), Évora (red squares), Cabo da Roca (grey  
883 crosses), Granada (black stars), and El Arenosillo (green circles). Vertical bars indicate the standard  
884 deviation of each yearly value at Palencia station.

885 **Figure 6.** Evolution of annual ARE at the four spectral ranges (ARE<sub>UV</sub> purple diamonds, ARE<sub>VIS</sub>  
886 red squares, ARE<sub>NIR</sub> green triangles, and ARE<sub>SW</sub> black circles) and AOD at 500 nm (blue stars)  
887 averaging the data from the six Iberian ground-based sites (only years with at least three sites  
888 considered). Dashed lines point out the linear trends (see text).

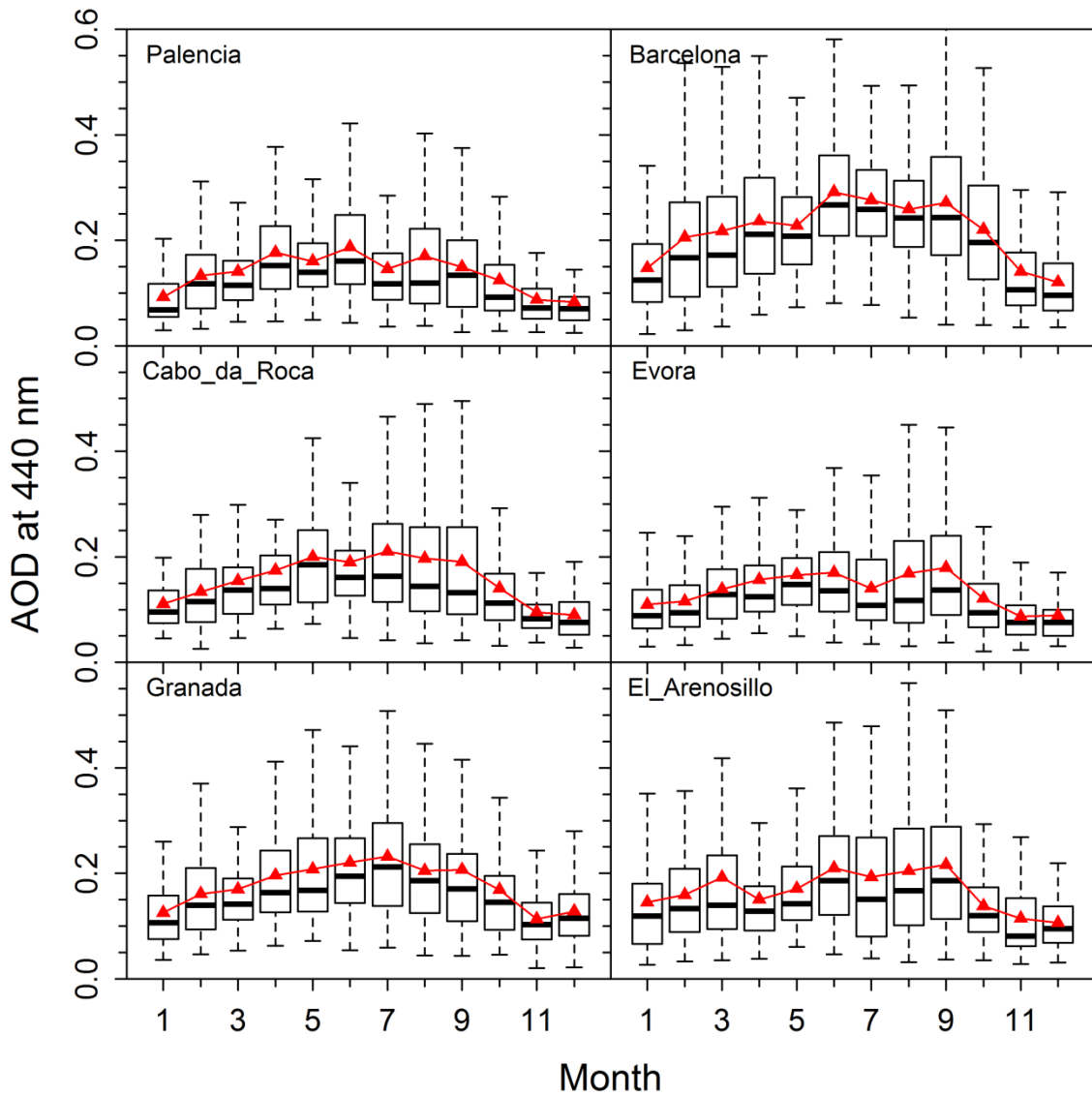
889 **Figure 7.** Annual cycle of ARE<sub>UV</sub> (a), ARE<sub>VIS</sub> (b), ARE<sub>NIR</sub> (c), and ARE<sub>SW</sub> (d) at the six sites:  
890 Barcelona (blue diamonds), Palencia (purple triangles), Évora (red squares), Cabo da Roca (grey  
891 crosses), Granada (black stars), and El Arenosillo (green circles). Vertical bars point out the  
892 standard deviation of each monthly value at Évora station.



893 **Figure 8.**  $AFE_{UV}$ ,  $AFE_{VIS}$ ,  $AFE_{NIR}$ , and  $AFE_{SW}$  against four groups of aerosol single scattering  
894 albedo and three intervals of  $\alpha$  at the six sites: Barcelona (blue diamonds), Palencia (purple  
895 triangles), Évora (red squares), Cabo da Roca (grey crosses), Granada (black stars), and El  
896 Arenosillo (green circles).

897 **Figure 9.** Dependence of  $AFE_{VIS}/AFE_{SW}$  (a, c, e) and  $AFE_{NIR}/AFE_{SW}$  (b, d, f) ratios on SSA for  
898 large (a, b), medium (c, d) and small (e, f) particles at the six sites: Barcelona (blue diamonds),  
899 Palencia (purple triangles), Évora (red squares), Cabo da Roca (grey crosses), Granada (black stars),  
900 and El Arenosillo (green circles).

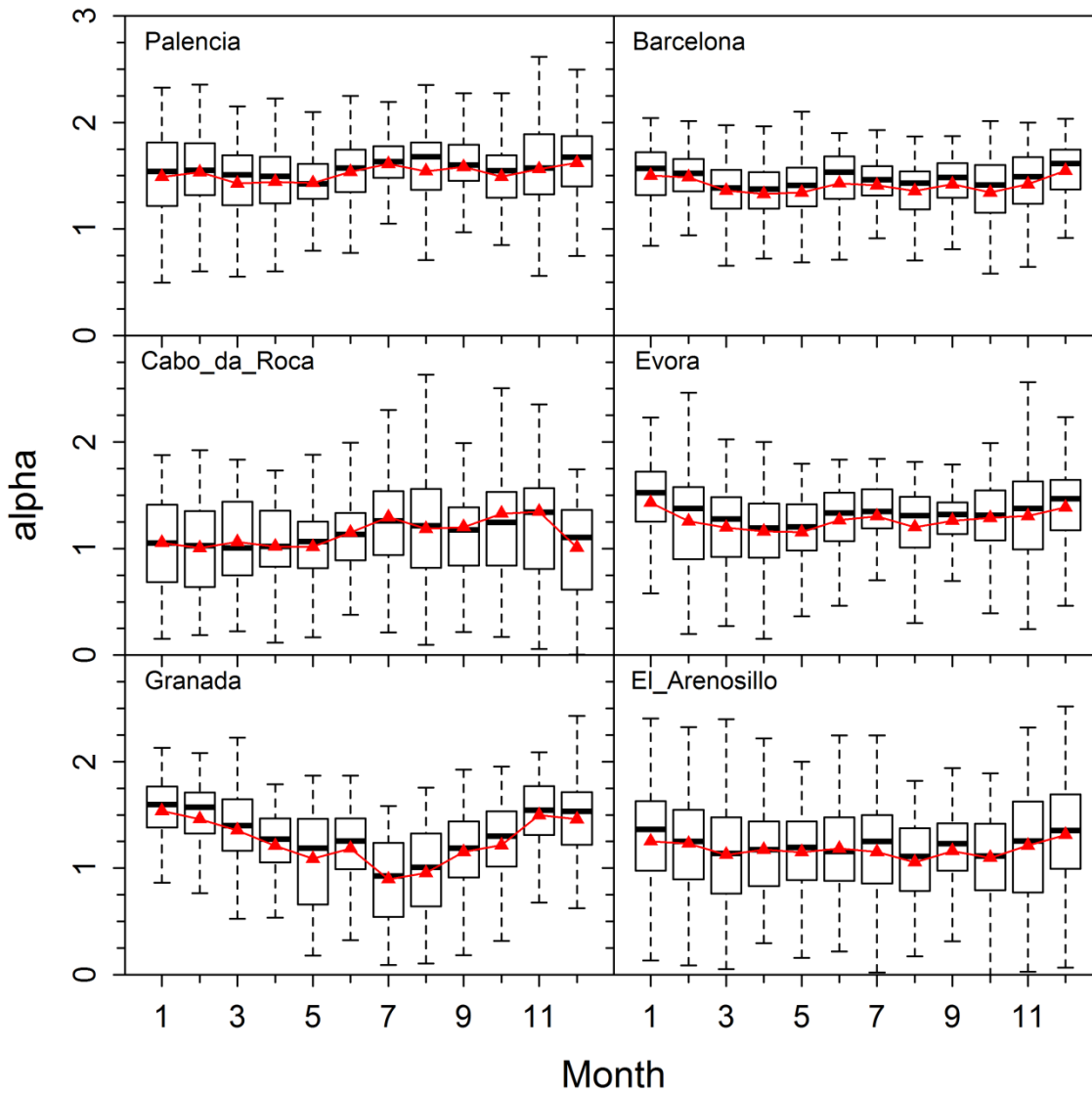
901



903

904 **Figure 1.** Annual cycle of daily values of AOD at 440 nm by box whisker plots. Triangles and  
905 horizontal solid lines indicate the monthly average and median values, respectively.

906



908

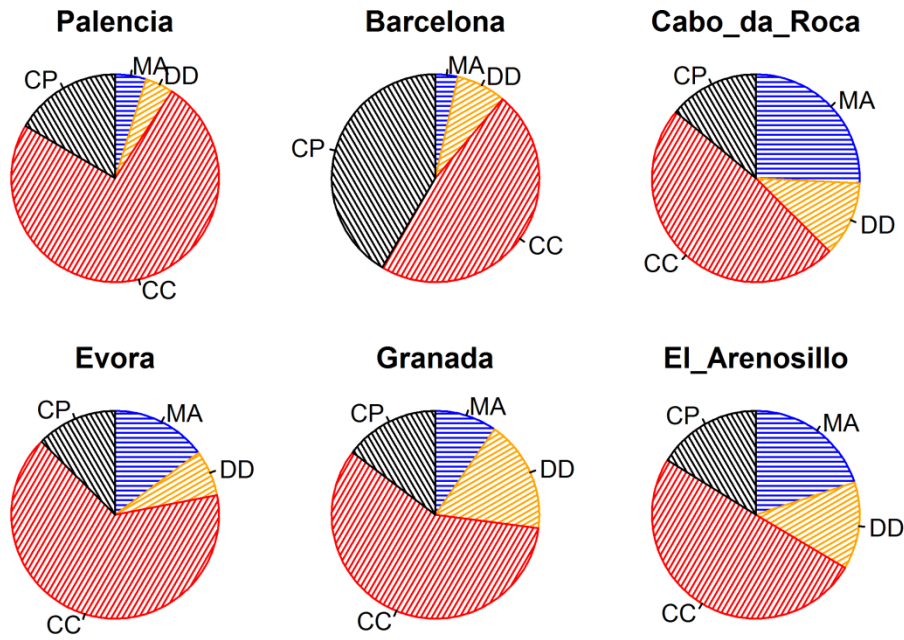
909 **Figure 2.** Annual cycle of daily values of  $\alpha$  ('alpha' in the figure) by box whisker plots. Triangles  
 910 and horizontal solid lines indicate the monthly average and median values, respectively.

911

912

913 Figure 3

914



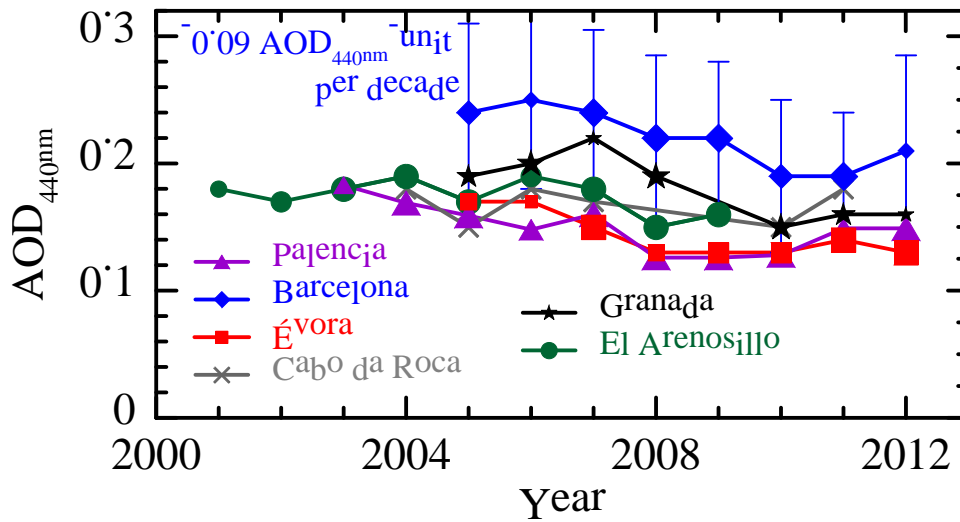
915

916 **Figure 3.** Relative frequency of aerosol type occurrence: maritime (MA), desert dust (DD),  
917 continental clean (CC), and continental polluted (CP).

918

919 Figure 4

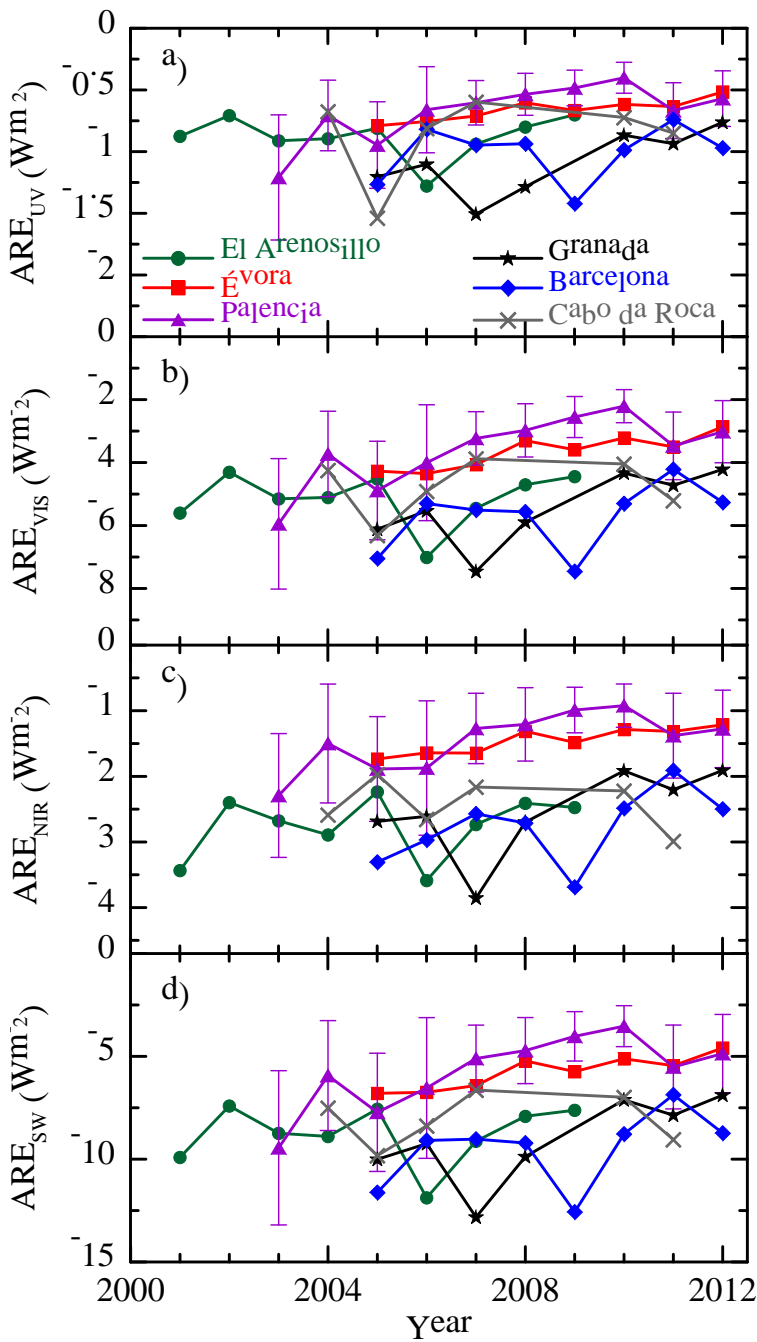
920



921

922 **Figure 4.** Yearly values of AOD<sub>440nm</sub> at the six sites: Barcelona (blue diamonds), Palencia (purple  
923 triangles), Évora (red squares), Cabo da Roca (grey crosses), Granada (black stars), and El  
924 Arenosillo (green circles). The text points out the statistically significant trend obtained. Vertical  
925 bars indicate the standard deviation of each yearly value at Barcelona station. Larger the symbols,  
926 large amount of data number that year (e.g., the smallest symbols indicate cases between 100 and  
927 150 points, while the largest symbols show years with >250 points).

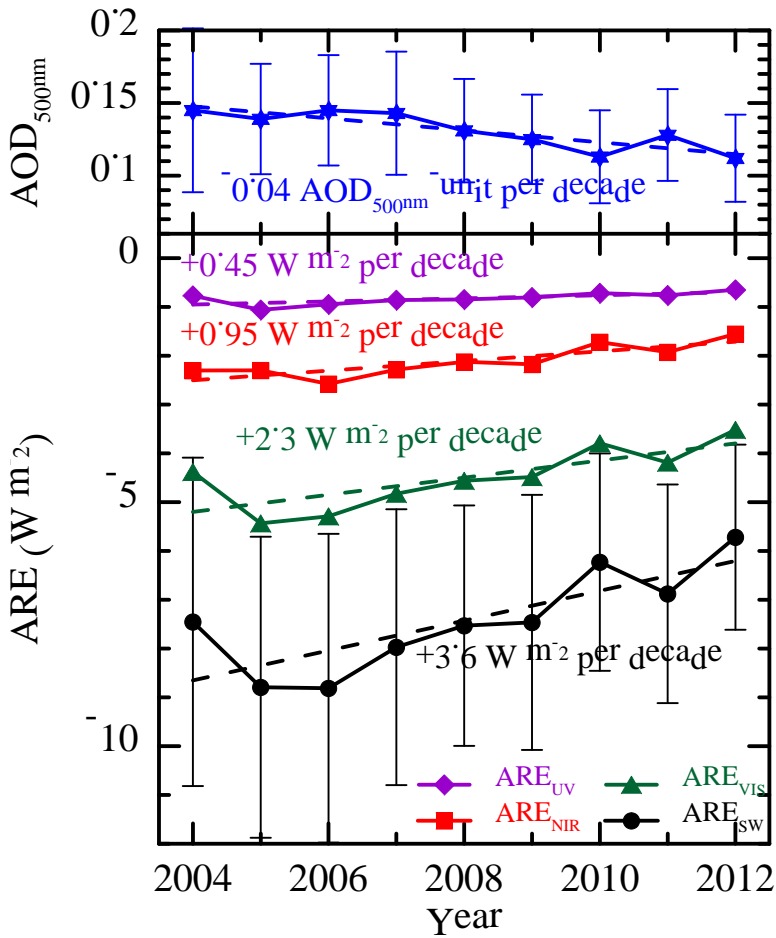
928



930

931 **Figure 5.** Evolution of yearly  $ARE_{UV}$  (a),  $ARE_{VIS}$  (b),  $ARE_{NIR}$  (c), and  $ARE_{SW}$  (d) at the six sites:  
 932 Barcelona (blue diamonds), Palencia (purple triangles), Évora (red squares), Cabo da Roca (grey  
 933 crosses), Granada (black stars), and El Arenosillo (green circles). Vertical bars indicate the standard  
 934 deviation of each yearly value at Palencia station.

935 Figure 6  
 936  
 937

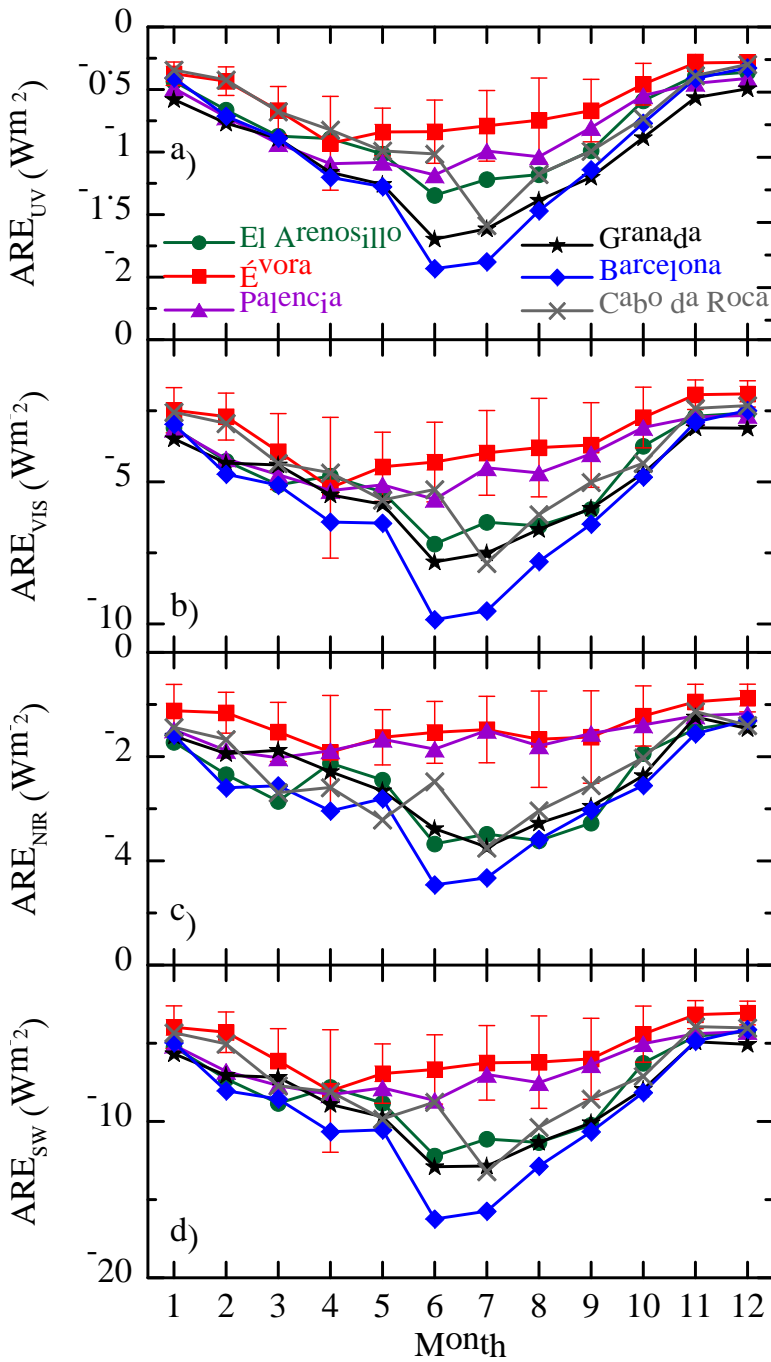


938  
 939

940 **Figure 6.** Evolution of annual ARE at the four spectral ranges ( $\text{ARE}_{\text{UV}}$  purple diamonds,  $\text{ARE}_{\text{VIS}}$   
 941 red squares,  $\text{ARE}_{\text{NIR}}$  green triangles, and  $\text{ARE}_{\text{SW}}$  black circles) and AOD at 500 nm (blue stars)  
 942 averaging the data from the six Iberian ground-based sites (only years with, at least, three sites are  
 943 considered). Dashed lines point out the linear trends (see text). Vertical bars indicate the standard  
 944 deviation.

945

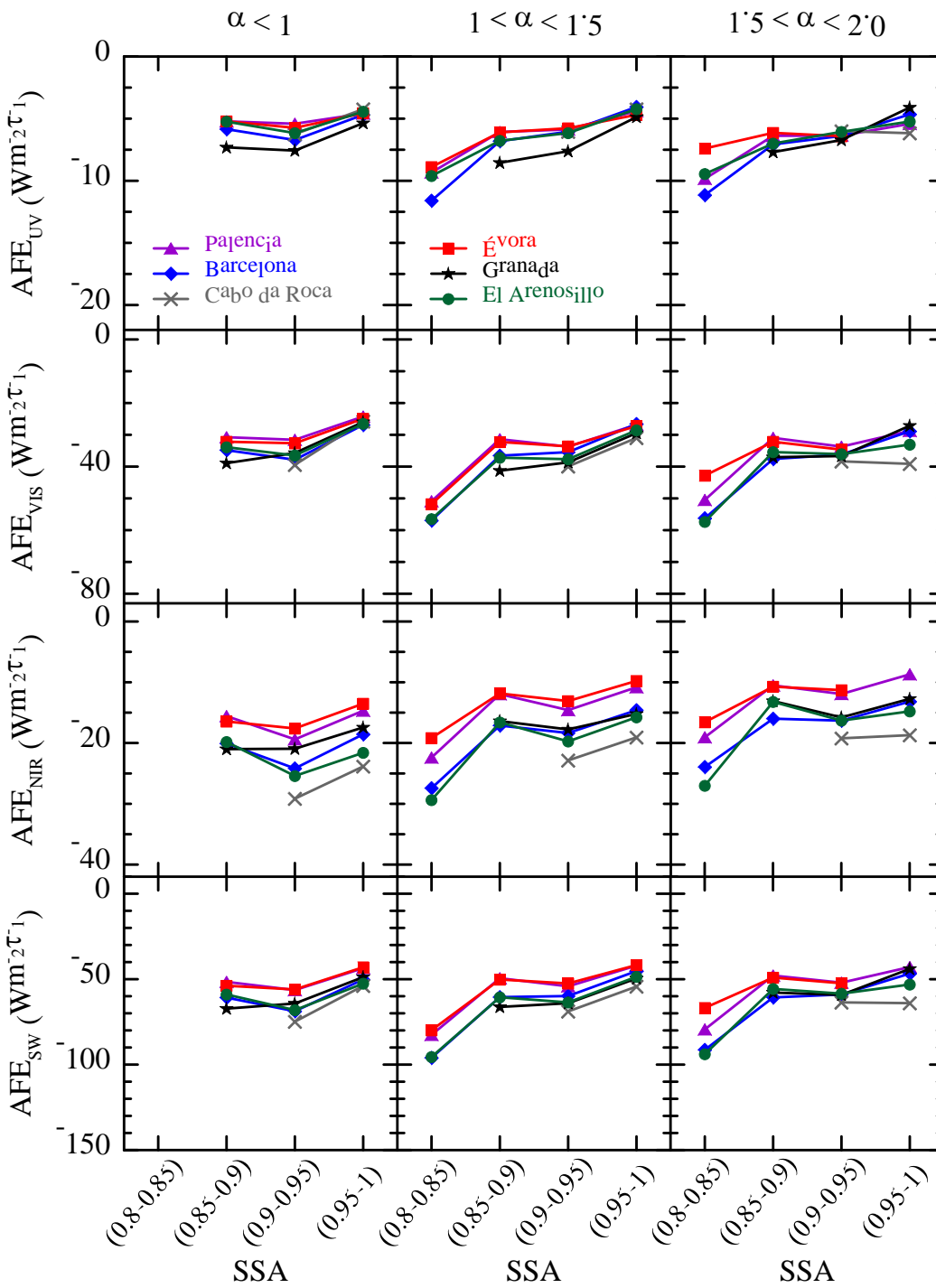
946 Figure 7  
947



948

949 **Figure 7.** Annual cycle of  $ARE_{UV}$  (a),  $ARE_{VIS}$  (b),  $ARE_{NIR}$  (c), and  $ARE_{SW}$  (d) at the six sites:  
950 Barcelona (blue diamonds), Palencia (purple triangles), Évora (red squares), Cabo da Roca (grey  
951 crosses), Granada (black stars), and El Arenosillo (green circles). Vertical bars point out the  
952 standard deviation of each monthly value at Évora station.



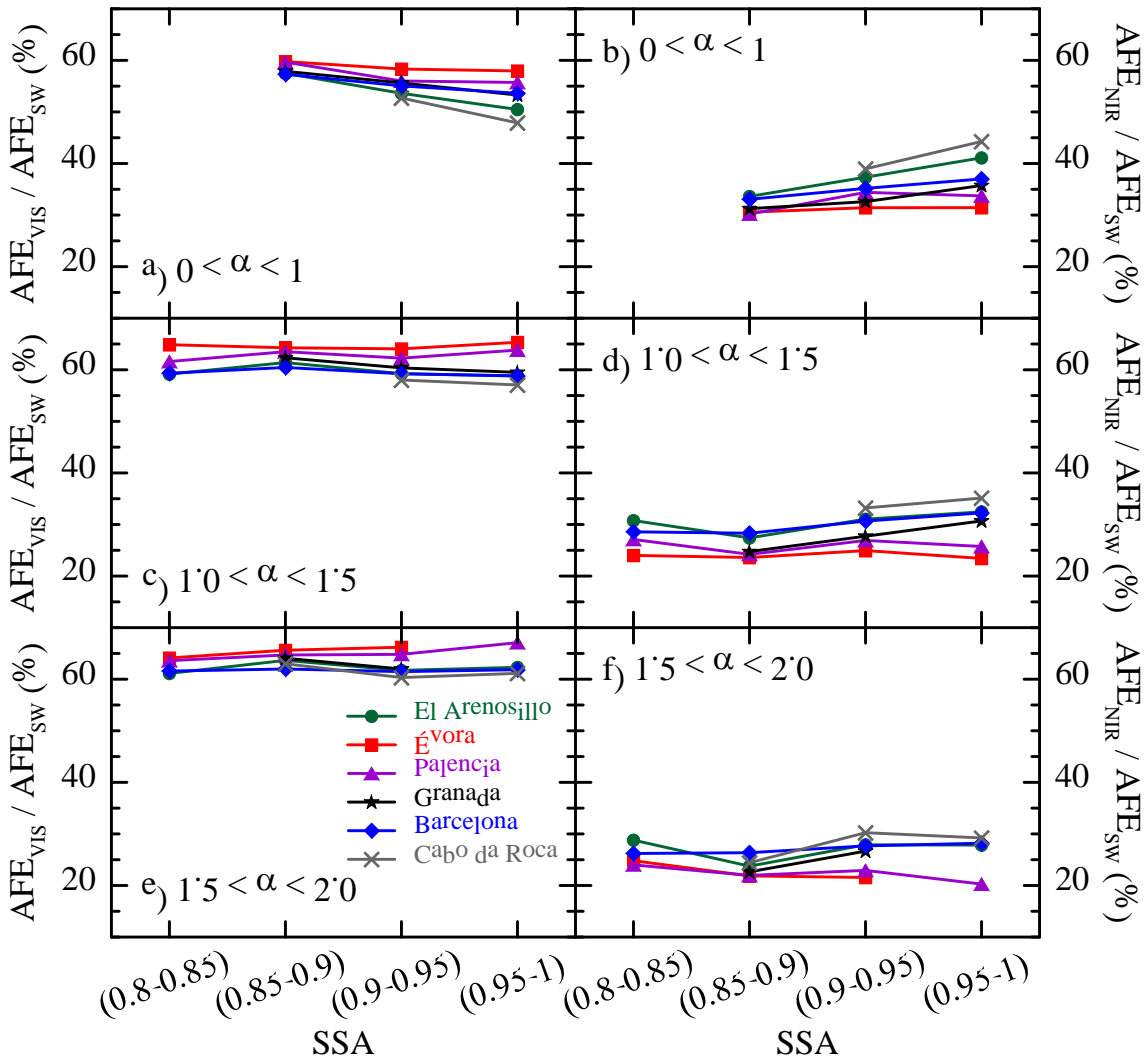


954

955 **Figure 8.**  $AFE_{UV}$ ,  $AFE_{VIS}$ ,  $AFE_{NIR}$ , and  $AFE_{SW}$  against four groups of aerosol single scattering  
 956 albedo and three intervals of  $\alpha$  at the six sites: Barcelona (blue diamonds), Palencia (purple  
 957 triangles), Évora (red squares), Cabo da Roca (grey crosses), Granada (black stars), and El  
 958 Arenosillo (green circles).

959 Figure 9

960



961

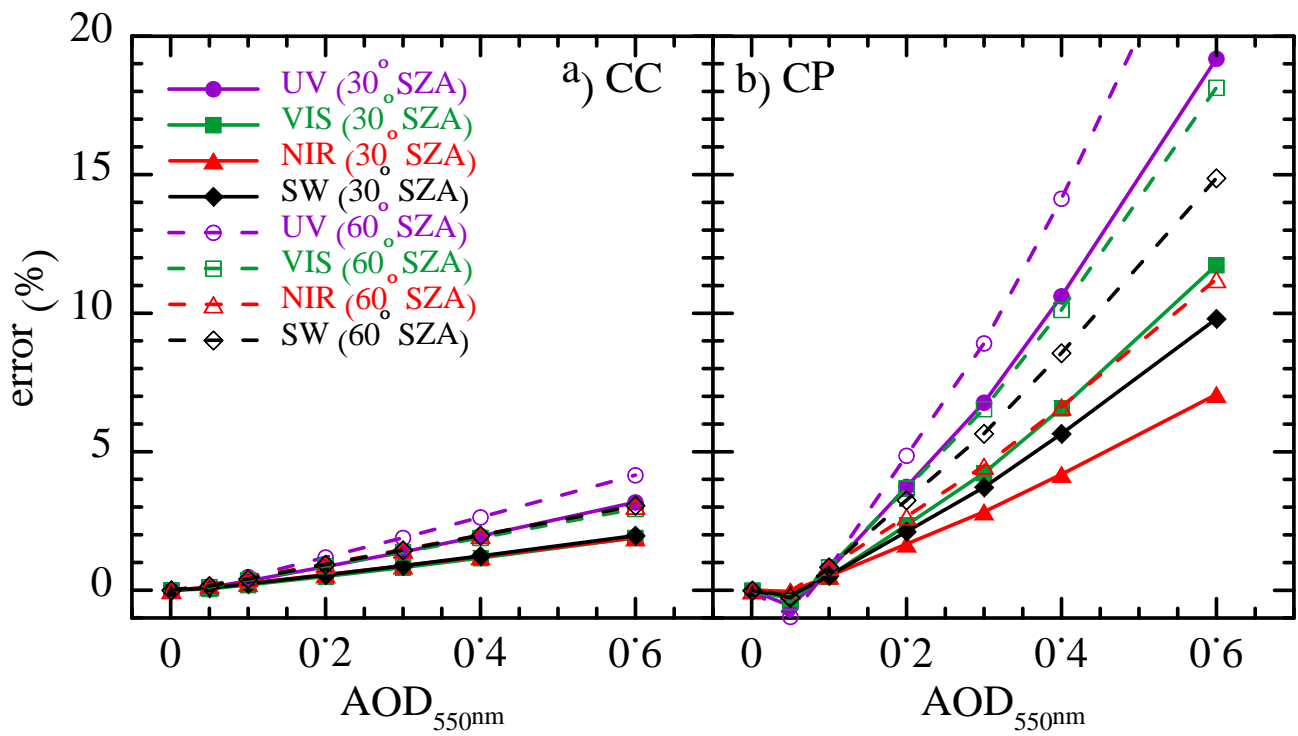
962 **Figure 9.** Dependence of  $AFE_{VIS}/AFE_{SW}$  (a, c, e) and  $AFE_{NIR}/AFE_{SW}$  (b, d, f) ratios on SSA for

963 large (a, b), medium (c, d) and small (e, f) particles at the six sites: Barcelona (blue diamonds),

964 Palencia (purple triangles), Évora (red squares), Cabo da Roca (grey crosses), Granada (black stars),

965 and El Arenosillo (green circles).

966



970 Figure A1. Dependence on aerosol load of the error committed when the optical properties are fixed  
 971 in the different spectral ranges for two SZAs (30° solid lines and symbols, and 60° dashed lines and  
 972 open symbols), and continental clean (CC, a) and continental polluted (CP, b) aerosols.